Master's Degree in Physics of the Universe

Universidad Zaragoza

Final Master's Thesis

Unraveling Neutron Star Secrets: Magnetar Studies using X-ray Telescopes

---

Author,

Francisco Rodríguez Candón

Director,

Julia K. Vogel

July 10, 2024

Abstract

Neutron stars (NSs) are the remnants of massive stars and exhibit extreme compactness, high density, rapid rotation, and strong magnetic fields. Among them, magnetars are a fascinating subset known for their extraordinarily strong magnetic fields and their unique X-ray and gamma-ray emissions. This thesis presents the development and application of software tools to analyze data from X-ray telescopes such as NuSTAR, Swift, and Chandra, focusing on the magnetar SGR J1745-29, located near the supermassive black hole SgrA* in the Galactic Center. The developed tools streamline the analysis process from raw data to scientific conclusions, enabling detailed spectral and temporal studies. By replicating previous findings and examining new data, this research investigates the temporal evolution of SGR J1745-29's properties, including a potential rise in its blackbody temperature. Additionally, the thesis explores the potential of magnetars as laboratories for axion research.

Contents

1 Introduction

Neutron stars (NSs) are stellar endpoints of massive stars (8-25 solar masses $M_{\odot}$), characterized by their extreme compactness, with typical radii of about 10 kilometers and densities exceeding 10^{17} kg/m^3. They also feature strong magnetic fields, typically ranging from 10^8 to 10^{15} Gauss. Neutron stars rotate rapidly, with periods commonly ranging from milliseconds to a few seconds. They encompass a wide variety of classes, with one particularly intriguing group being magnetars, which are notable for their extraordinarily strong magnetic fields, typically ranging from 10^{13} to 10^{15} G. Only 30 magnetars are currently known to exist (see McGill magnetar Catalog [1]), making them a rare and fascinating subset of NSs. Magnetars were first proposed by Robert C. Duncan and Christopher Thompson in 1992 [2], in order to explain the behaviour of two NSs sub-classes initially thought to be completely distinct, namely soft gamma repeaters (SGRs) and anomalous X-ray pulsars (AXPs). In the magnetar scenario, the two sub-classes are considered to be at different ends of a continuous activity spectrum. Their distinctive characteristics include intermittent bursts of X-rays and soft gamma rays, accompanied by luminosities that frequently exceed what would be anticipated from their spin-down-powered X-ray emission. Typical spin periods for magnetars lie in the range $P = 2.1 - 11.8$ s, and spin-down rates of the order of $\dot{P} = 10^{-11}$ s s^{-1}. Magnetars are assumed to be rather young, since the characteristic ages τ of these objects ($\tau = P/2\dot{P}$) are of the order of thousands of years.

The discovery and study of magnetars was primarily enabled by ground-breaking advances in the development of space-based X-ray telescopes during the last 50 years. The soft X-ray spectrum (0.3-10 keV) is the best studied thanks to observatories like Chandra [3] or Swift [4]. Thermal emission from the neutron star surface (blackbody emission) is a dominant component in explaining the soft X-ray spectra of magnetars, magnetospheric processes can also play a role, especially in shaping the non-thermal aspects of the X-ray emission starting towards the higher end of the soft band as a subdominant component often well described by a powerlaw. On the other hand, the hard X-ray spectrum (> 10 keV) has been observed by telescopes such as INTEGRAL, Suzaku, and by the only focusing telescope in this energy range, NASA's Nuclear Spectroscopic Telescope Array (NuSTAR, [5]). Above 10-15 keV, the magnetar spectrum often includes a combination of thermal emission from the neutron star surface (blackbody component at the lower end of energies) and non-thermal emission processes associated with magnetospheric activity (at higher energies). Typical spectral characteristics for non-thermal emission usually include a power-law or hard tail component. This suggests that the X-ray emission above 10-15 keV is not solely due to thermal radiation from the neutron star surface but rather originates from processes in the magnetosphere that accelerate particles to high energies. Typically, observations in the hard X-ray regime suffer from lower statistics than in the soft energies, given that NuSTAR is the only available instrument that can provide us with sufficient spectral resolution and sensitivity in this energy range.

One of the most interesting magnetars to study is SGR J1745-29, situated in the Galactic Center and gravitationally bound to the Milky Way's supermassive black hole SgrA*, only 2.4" away. It was first discovered due to bursting activity in April 2013 by the Swift X-ray observatory [6] and the NuSTAR satellite [7]. The spin period of SGR J1745-29 is $P = 3.76$ seconds and its derivative $\dot{P} = 6.5 \times 10^{-12}$, which implies a magnetic field of $B = 1.6 \times 10^{14}$ G. Two follow-up papers were published after the discovery, a 5-month NuSTAR data study after the outburst [8], and a 3.5 years Chandra monitoring campaign of the soft X-ray band

[9]. Chandra observations prove especially crucial for studying the spectral variations of SGR J1745-29, since its high angular resolution of 0.5" allow us to resolve the magnetar unequivocally avoiding source confusion with SgrA* and excluding contamination coming from outer sources in this highly X-ray active region.

The main objectives of this thesis are the creation of software tools and their application to study basic magnetar properties. First, we created a programming environment which allows for the study and analysis of observational data from X-ray telescopes, specifically from NuSTAR, Swift and Chandra. While many mission tools are readily available, putting together a full analysis path is not straightforward. For this purpose, tutorials for each specific tool were made and code was written to enable a simple start-to-finish analysis from raw data to final science product.

In a second step we applied the programming tools developed earlier to study of basic magnetar properties via spectral and temporal analysis and the evolution of the results over time. Specifically, we focus on the study of magnetar SGR J1745-29, which will be used, first, to test all developed routines by reproducing the results published previously in the magnetar discovery and follow-up papers that use data from Swift and NuSTAR ([7], [8]). Then we will analyze additional data to study the evolution of magnetar features with time and to follow up on a potential hint towards an unexpected increase in the blackbody temperature (kT) of SGR J1745-29 using recent NuSTAR data [10]. We use the Chandra telescope, whose 0.5" will allow us to discard any possible contamination from X-ray transients that may have appeared close enough to the source to not be distinguishable in the NuSTAR data while contaminating the blackbody temperature measurement.

Before concluding we will briefly discuss the possibility of using magnetars as stellar laboratories to search for dark matter in the form of axions.

2 Neutron Stars and Magnetars

Neutron stars (NS) are remnants of supernova explosions that a star with a mass between 8 and 25 solar masses ($M_\odot$) undergoes when its nuclear energy can no longer counteract gravitational collapse. NSs are extremely dense objects with a mass around 1.5 $M_\odot$, a radius of approximately 10 km, and a central density (n_c) reaching 5 to 10 times the nuclear equilibrium density of neutrons and protons found in laboratory nuclei. This makes neutron stars some of the densest forms of matter in the observable universe. While neutrons dominate the composition of neutron stars, these stellar objects also contain some protons, along with enough electrons and muons to ensure charge neutrality. At densities exceeding nuclear levels, exotic particles such as strangeness-bearing baryons, condensed mesons (like pions or kaons), or even deconfined quarks might emerge. Furthermore, fermions, whether in the form of hadrons or deconfined quarks, are expected to exhibit superfluidity and/or superconductivity [11].

Back in the 60s, the discovery of radio pulsar was immediately associated with neutron stars, being the only stellar objects capable of rotating this rapidly. The development of high-energy space telescopes in the past 50 years has allowed us to recognize the existence of other manifestations of non-accreting NS . Specifically, there are two sets of X-ray pulsars with peculiar properties; the Anomalous X-ray Pulsars (AXPs) and the Soft Gamma Repeaters (SGRs). AXPs were called anomalous because their high luminosity ($\sim 10^{34} - 10^{36}$ erg$/s$) can not be easily explained in terms of the processes that are common in other pulsars. On the other hand, SGRs were identified with periodically intense bursts in the hard X-/soft gamma-ray range. In the early 2000s, the similarities between the two became so clear that a unique class of NS emerged uniting both of these NS categories, the magnetars.

The term magnetar was first introduced by Robert C. Duncan and Christopher Thompson in 1992 [2], referring to a NS whose X-ray emission is powered by the decay of its enormous internal magnetic fields. The author's arguments were based on the location of the 8-sec pulsar SGR 0526-66 in the Large Magellanic Cloud (LMC) supernova remnant N49. Typically, the proto-NS created after a supernova event has a period of the order of a few milliseconds rather than secs. As a consequence, a surface dipolar magnetic field of the order of $10^{14} - 10^{15}$ G was required to slow-down the pulsar from millisecond to 8 seconds in the usual lifetime of a supernova remnant (SNR) $\sim 10^4$ yrs. In addition, such a huge magnetic field could provide the necessary energy to explain the SGR event. Rotation of these objects must be slowing down, because lower periods and higher magnetic fields could break the star. The spin-down rate was later confirmed by Ref. [12] for the source SGR 1806-20, for which the surface dipolar magnetic field at the poles was estimated (assuming a magnetic dipole braking) as

$$B_p \approx 3.2 \times 10^{19} \sqrt{P\dot{P}}\ \mathrm{G} = 3.2 \times 10^{19} \sqrt{7.47s \cdot 8.239 \times 10^{-11} ss^{-1}} \sim 8 \times 10^{14}\mathrm{G} \tag{1}$$

where P is the period and $\dot{P}$ its derivative (see Appendix A for the full derivation of the dipolar magnetic field at the poles). In parallel, a "new extraordinary celestial X-ray source" (as it was called in their article) was discovered by P.C. Gregory [13] using the Einstein Observatory, a 7-sec X-ray source in the supernova remnant CTB 109. Later in the decade, two more sources of this kind were discovered, however, this time not inside a SNR. All three had unusual periods of a few seconds and soft X-ray spectra, features that had been observed previously in low-mass X-ray binaries. However, the fact that they were isolated pointed to a new class of pulsars, dubbed AXPs. A few years after the proposal of the initial magnetar model, Ref. [14] suggested a relation between AXPs and SGRs, expecting that in the future SGRs events were going to be observed in AXPs sources, something that was confirmed in the early 2000s.

In the following, we summarize the main arguments that support the idea that SGRs and AXPs are indeed powered by enormous magnetic fields within the magnetar scenario:

- The rotational energy loss $\dot{E}$ is believed to fuel standard pulsars, however, for magnetars it is much lower than the persistent X-ray luminosity.
- Since some of these objects have been found in supernova remnants ($10^3 - 10^4$ yrs after the supernova), the characteristic long periods $\sim 5 - 10$ s can only be achieved via magneto-dipolar braking for $B \sim 10^{14} - 10^{15}$ G.
- To date, all confirmed magnetars are not part of binary systems, which rules out accretion as the source of their phenomena.
- An internal field of $\sim 10^{16}$ G is needed to power the ~ 100 giant flares, like the ones emitted in 2004 by SGR 1806-20, over the lifetime of a magnetar.

The spin-down of magnetars is highly irregular and often accompanied by glitches (sudden, irregular decreases in the rotational period) and timing noise. Long-term variations in magnetar emissions can manifest either as gradual, moderate changes in flux, accompanied by alterations in the spectrum, pulse profile, and spin-down rate, or as sudden outbursts. These outbursts can increase the flux by a factor of up to ~ 1000, followed by a decay back to a level consistent with the quiescent state over a timescale of months to years.

To date, only 24 SGR/AXPs have been confirmed as magnetars[a], 6 more remain candidates. Given the limited statistics, our understanding of these objects remains constrained, making spectral and timing analyses over time crucial for uncovering the intriguing physics of magnetars.

2.1 Magnetar Formation

In the model proposed by Robert C. Duncan and Christopher Thompson [2], ultra-magnetized neutron stars are formed through the amplification of magnetic fields by a powerful dynamo action during the early and highly convective stages. Two processes can enhance dynamo effects in plasma: rotation and convection. The α dynamo arises from the coupling of convective motions and rotation, and the w dynamo from the differential rotation. Both effects are present in proto-neutron stars, where the rapid rotation leads to a low Rossby number, a dimensionless parameter that quantifies the relative importance of inertial forces in a rotating fluid system. For the Coriolis forces to efficiently influence convective motions and enhance dynamo action, amplifying the magnetic fields, the initial periods of proto-neutron stars must be $\lesssim 3$ ms. Magnetars might therefore represent the final stage in the evolution of massive stars with rapidly rotating cores.

Alternatively, it has been proposed that ultra-strong fields in neutron stars result from magnetic flux conservation, known as the fossil field scenario Ref. [15]. Using the 1374-MHz Parkes Multi-Beam Survey, it was found that about 8% of OB[b] progenitor stars have core magnetic fields exceeding 1000 G. Their core-collapse can produce around 25 magnetars of properties consistent with those observed in SGRs and AXPs. This is further supported by the observational evidence that some magnetars are associated with young clusters of massive stars. One of the strongest pieces of evidence supporting high-mass progenitors for SGRs and AXPs is the robust association of AXP CXO J164710.2-455216 with the young cluster Westerlund 1. Given that the cluster is only approximately 4 million years old, the minimum mass of a star that could have reached the supernova stage is around $40M_{\odot}$, which suggest that it originated from a star with these characteristics. There is something groundbreaking in this hypothesis: high-field OB progenitors, with masses around $20-45M_{\odot}$, are predicted by stellar evolution models to lead to black holes through the formation of a fallback disc [16].

More recently, it was proposed that the magnetar CXO J164710.2-455216 was born in a massive binary system, where the companion was ejected after the progenitor's supernova [17]. Evidence was found suggesting that the runaway star Wd1-5 was the ejected former companion. If Wd1-5 and CXO J164710.2-455216 are indeed connected, the binary evolution would have caused the progenitor's mass to decrease significantly due to strong mass loss during its Wolf-Rayet phase, when stellar winds are extremely powerful, stripping away part of their mass[c]. Additionally, the Wolf-Rayet star might enter a common envelope phase, where the envelope of the star engulfs the companion, leading to additional mass loss to the progenitor and preventing the core from spinning down. Thus, the birth of a magnetar in a binary system might be crucial for reducing the progenitor's mass to fall within the neutron star formation range, and for maintaining the

---

[a] McGill Online Magnetar Catalog

[b] OB stars are among the hottest, most massive, and brightest stars, classified under the O and B spectral types. They have high surface temperatures (10k-30k Kelvin), are very luminous, and emit significant ultraviolet radiation.

[c] Watch this video for an illustrative approach.

high core rotational speed necessary for initiating the convective dynamo.

2.2 Magnetospheric Twist

A significant challenge in the study of neutron stars (and magnetars in particular) is that observations provide minimal, if any, constraints on the structure and strength of their internal magnetic fields. Over the past decade, analytical and numerical studies have demonstrated that any stable configuration of a star's internal magnetic field must include both poloidal and toroidal components. Braithwaite et al. [18] explored stable, axisymmetric magnetic equilibrium and found that the toroidal component must be at least of the same order, and possibly stronger, than the poloidal one. Numerical solutions for stationary and axisymmetric relativistic rotating stars with strong mixed poloidal and toroidal magnetic fields have been achieved by Ref. [19].

In magnetars, internal fields can exceed 10^{15}G, and magnetic stresses can be sufficient to break or deform the magnetar crust. The easiest way for the crust to respond to magnetic stresses is by moving horizontally, along the magnetic equipotential surfaces. This horizontal displacement causes areas of the crust to rotate by a certain angle $\Delta\phi$ and can be understood by considering a flux tube where the toroidal component is present within the crust but disappears outside the star (See Figure 1). Due to the high conductivity in the star's interior, the electric currents that support the non-potential magnetic field close in a thin surface layer just below the star's crust ΔR_0. The Lorentz force that the currents, and hence the layer, will experience is:

$$\vec{F}_{\rm L} = \frac{1}{c}\vec{j} \times \vec{B} = \frac{1}{c} j \times \left(\vec{B}_{\rm p} + \vec{B}_{\rm t}\right) \tag{2}$$

where $\vec{j}$ is the current density, and $\vec{B}_{\rm p}$ and $\vec{B}_{\rm t}$ correspond to the poloidal and toroidal magnetic field components. The part of the Lorentz force arising from the toroidal component tries to displace the surface layer vertically, which is unlikely to occur due to strong stratification (the density gradient increases dramatically as one goes deeper into the neutron star). On the other hand, the B-field part associated with the poloidal component results in a slippage in the horizontal direction (See Figure 1). Since the external magnetic field lines are anchored to the crust, this torsional displacement of the surface layers leads to a twist in the external field lines. This process results in the transfer of magnetic helicity, a variable which measures the twist and complexity of the field lines, from the star's interior to its exterior. If the external field was initially dipolar, this effect will produce a toroidal component, aka a twist.

In a twisted magnetosphere, currents must flow along the closed field lines to sustain the non-potential field, which contrasts with the usual approach to radio-pulsars, where charges move only along the open field lines. The proposed scenario assumes a gradually increasing twist, which leads to a higher optical depth for resonant cyclotron scattering and progressively hardens the X-ray spectrum. Simultaneously, the spin-down rate is expected to increase because, for a constant dipole field, a larger fraction of the magnetic field lines extends beyond the speed-of-light cylinder.

The magnetospheric twists are expected to be localized, without affecting the whole magnetosphere. However, magnetar property studies usually assume a 'globally twisted magnetosphere' [21]. In this model, it is assumed that the external magnetic field starts as dipolar B-field. However, due to displacements of the crust, the field experiences added shear. When considering magnetostatic equilibria in a low-density plasma, the momentum equation simplifies to $\vec{j} \times \vec{B} = 0$

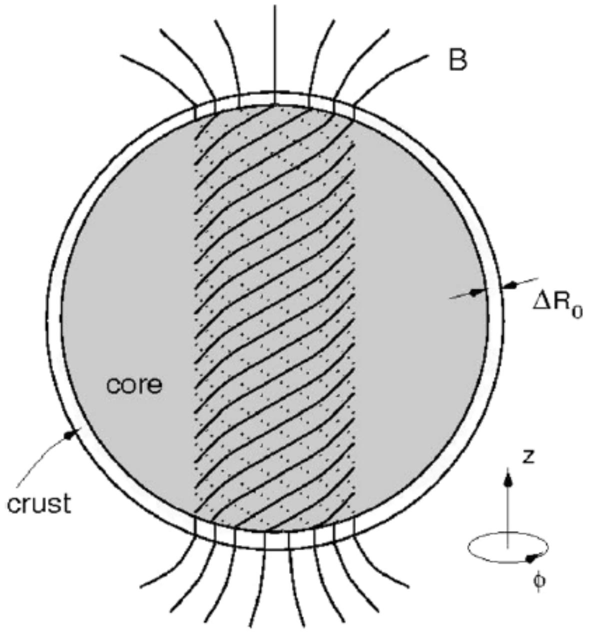

Figure 1: Illustration of a magnetar's internal magnetic field structure: an almost spherical star is threaded by a uniform poloidal magnetic field, which extends through both the liquid core and the solid outer crust. Within the core, this field is twisted, generating a toroidal component. From Ref. [20]

(since magnetars are slow rotators, Coulomb force is negligible in the inner magnetosphere), for which in combination with the Ampère-Maxwell equation $\vec{\nabla} \times \vec{B} = (4\pi/c)\vec{j}$, one can substitute $\vec{j}$:

$$\vec{j} \times \vec{B} = \frac{4\pi}{c}(\nabla \times \mathbf{B}) \times \mathbf{B} = 0 \longrightarrow (\nabla \times \mathbf{B}) \times \mathbf{B} = 0, \tag{3}$$

which represents the force-free condition. By representing the poloidal component using the flux function $\boldsymbol{\mathcal{P}}$, the most general form of an axisymmetric field is given as

$$\vec{B} = \frac{\nabla \boldsymbol{\mathcal{P}}(r,\theta) \times \vec{u}_\phi}{r \sin\theta} + B_\phi(r,\theta)\vec{u}_\phi, \tag{4}$$

where B_ϕ is the toroidal component and $\vec{u}_\phi$ is the unit vector in the ϕ direction. It should be noted that r is the radial distance taking the center of the NS as a point reference, and θ is the polar angle using the rotational axis as a reference. By utilizing the force-free condition, the magnetic field can be explicitly expressed as follows:

$$\vec{B} = \frac{B_p}{2}\left(\frac{r}{R_{\mathrm{NS}}}\right)^{-p-2}\left[-f', \frac{pf}{\sin\theta}, \sqrt{\frac{Cp}{p+1}}\frac{f^{1+1/p}}{\sin\theta}\right], \tag{5}$$

where B_p is the magnetic field value at the pole, R_{NS} is the NS radius, the prime denotes a derivative with respect to $\mu \equiv \cos\theta$, C is a constant and $0 \leq p \leq 1$ is the radial index. The function $f(\mu)$ satisfies the Grand-Shafranov equation:

$$\left(1-\mu^2\right) f'' + p(p+1)f + Cf^{1+2/p} = 0, \tag{6}$$

which represents a second-order ordinary differential equation for the angular component of the flux function (For the full development see [21, 22]). The solution of the last equation, determines the external magnetic field completely.

2.3 Current Distribution

As we just mentioned, one can regard a twisted magnetosphere as a force-free configuration interwoven by currents flowing along the B-field lines. The enormous magnetic field extracts charges from the star's surface, which are then accelerated by the electric field parallel to $\vec{B}$. Electrons and ions must be moving in opposite directions in order to ensure charge neutrality. To achieve a current density parallel to the magnetic field, the electrons must move very quickly, requiring a high Lorentz factor (about $\gamma \approx 10^9$). However, as the electrons gain this much energy, they interact with the strong magnetic field around them. This interaction leads to a process called one-photon pair production through resonant cyclotron up-scattering. In this process, the electrons, due to their high energy and the strong magnetic field, produce electron-positron pairs before their Lorentz factor can become extremely large. Because of this efficient pair production mechanism, the currents in the magnetosphere are mostly carried by these electron-positron pairs, rather than individual electrons. The magnetosphere reaches a state of self-organized criticality, meaning it naturally stabilizes at a critical point where small changes can trigger large-scale events, like pair cascades. The voltage drop in the magnetosphere is close to the level required to start these pair cascades, maintaining a delicate balance [22].

2.4 Magnetar Spectrum

2.4.1 Soft X-Ray Spectrum

The soft X-ray band corresponds to energies between 0.3 and 10 keV. It is the best studied, thanks to telescopes like Chandra, SWIFT and XMM that have been studying this band for decades. The observed spectra are typically modeled using a double-component approach, consisting of a thermal component (a blackbody at ~ 0.5 keV) and a steep power law (photon index $\sim$ 3–4) [23]. In some cases, such as the notable example of AXP XTE J1810-197, good spectral fits are also achieved with two blackbody components. The thermal component dominates in the lower energy band, and the power-law component start to dominate just below 10 keV. It has been widely suggested that the blackbody plus power-law spectra can be explained by the soft, thermal emission from the neutron star's surface being distorted by the resonant cyclotron scattering (see Subsec. 2.3) on magnetospheric charges. As electrons occupy a spatially extended region of the magnetosphere with varying magnetic fields, resonant scattering is expected to produce a hard tail superimposed on the seed thermal bump, rather than narrow lines [24]. Numerous teams have conducted simulations that reproduce observational data quite accurately (For a comprehensive review, see [22]).

2.4.2 Hard X-Ray Spectrum

The hard X-ray band corresponds to energies greater than 10 keV and has been observed by telescopes such as INTEGRAL, RXTE, Suzaku, and NuSTAR, with NuSTAR being the first focusing telescope in this range.

In several magnetars, hard X-ray tails characterized by power-law spectra with photon indices $\Gamma \sim 0.5 - 2$ have been observed, indicating a flatter power law in this energy range than in the soft one. The intensity of these hard components can vary, but their luminosity is generally comparable to or greater than that measured at energies below 10 keV. Even in magnetars where hard X-ray emission has not been detected, the upper limits on detection do not rule out a significant contribution to the total luminosity. Notably, the pulsed emission within these hard X-ray tails often exhibits a harder spectrum than the averaged hard X-ray emission and shows phase-dependent variations. The origin of the hard X-ray tails in magnetars is still not well understood, but a commonly suggested mechanism involves up-scattering, similar to what has been proposed for their soft spectra [25].

3 X-ray telescopes

UHURU, [26], the first ever satellite dedicated to X-ray astronomy, was launched in 1970 from Kenya, into an equatorial orbit and operated for just 2 years. Using mechanically-collimated gas-filled detectors and a narrow field of view (FoV) of $0.5^\circ \times 0.5^\circ$, UHURU scanned the sky producing a catalogue of 339 X-ray sources, inlcuding X-ray binaries, supernova remnants (SNRs), galaxy clusters, and active galactic nuclei (AGNs).

The success of UHURU prompted the scientific community to advance towards a new generation of X-ray telescopes, in which the detector was positioned in the focal plane of an X-ray focusing device. Multiple background sources can affect the detection in this energy regime: cosmic rays, typically trapped particles in the Earth's radiation belt or gamma-rays secondary particles, and the diffuse isotropic cosmic X-ray background radiation. The sensitivity of the detector is $S/\sqrt{S+B}$, and taking into account that the background typically dominates this reduces to $S/\sqrt{B}$. Both, the source and the background, scale with the area, and therefore the sensitivity goes as $\sqrt{A}$, which means that to double the sensitivity one need the area to be 4 times larger [27]. However, the addition of an X-ray mirror to the setup focuses the X-ray flux onto a narrow detection area, significantly lowering the background and markedly enhancing the signal-to-noise ratio. This setup effectively separates the source and background fluxes; the source flux can be boosted by expanding the collecting area of the mirror (while maintaining a constant angular resolution and focal length). Additionally, reducing the size of the focal spot on the detector can further decrease the background making CCDs omnipresent in X-ray astronomy.

3.1 Challenges in Manufacturing X-ray Optics

While clearly advantageous, focusing X-rays is not quite as simple as focusing visible light. High-energy photons are easily absorbed by any material even for large incidence angles, i.e. the angles between incoming photons and the surface normal. For metals, the refractive index is just below one, such that total external reflection can take place at the surface of the material enableing X-ray reflection for large angles of incidence or respectively small grazing angles. Dispersion theory provides the critical angle, for which total reflection occurs, as approximately:

$$\theta_r^2 \propto r_0 \lambda^2 N_e, \tag{7}$$

where r_0 is the classical electron radius, N_e the electron density and λ the wavelength of the X-ray. The largest 'graze' angles occur with the most dense materials and at large λ (i.e. small X-ray photon energies E). Typical values for grazing angles are less than 1° for Iridium or Gold over the energy range between 1 and 10 keV. In order to enhance reflectivity and avoid

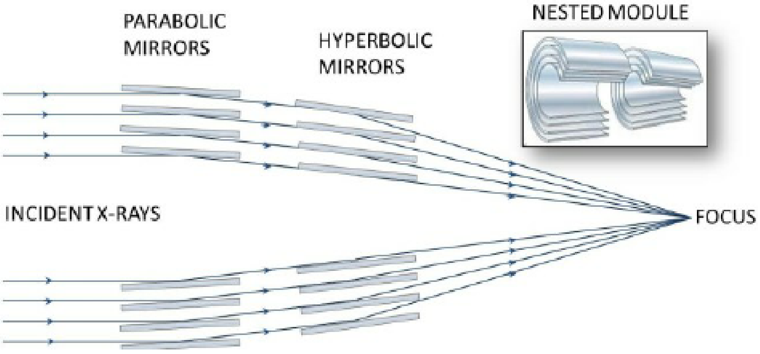

Figure 2: Wolter-I configuration of nested mirrors (From [27])

contamination, vacuum deposition is used to deposit these and other high Z materials on the surface of the mirror substrates.

Making use of the effect of total external reflection, one can create an X-ray optics using a certain configuration of mirrors in order to obtain a sharp image over a significantly-sized FoV. In 1960, Riccardo Giacconi proposed to use parabolic mirrors arranged in cylindrical cross sections [28]. This provides a very good on-axis resolution, however, the off-axis performance was strongly affected by coma. However, Hans Wolter proposed a configuration of a first segment of parabolic mirrors followed by a second segment of hyperbolic mirrors, the Wolter-I geometry [29]. This mirror configuration significantly enhanced off-axis performance, making it the optimal choice for the newer generation of X-ray telescopes. Due to the shallow graze angles, the mirror collecting areas are quite small, and extending the mirror shells too much would significantly degrade the angular resolution. Therefore, multiple mirror shells with the same focal length are nested concentrically to increase the effective area, as shown in Figure 2. The above-mentioned X-ray coatings can be used to further enhance reflectivity.

Irregularities in the mirrors can lead the X-rays to deviate from their expected trajectory. Low-frequency defects impact the overall geometric accuracy of the mirror, while high-frequency irregularities affect the surface roughness, leading to energy-dependent scattering. For optics with a few-arcsecond resolution, the figure accuracy at mid spatial scales (10 mm) must be around 0.1 microns. X-ray optics surfaces must be extremely smooth, matching the wavelength of the X-ray photons, to ensure efficient specular reflection. This makes the surface smoothness requirements for X-ray optics far more demanding than for visible light optics.

3.2 Nuclear Spectroscopic Telescope Array (NuSTAR)

The *Nuclear Spectroscopic Telescope Array* (NuSTAR) is the first focusing space telescope to extend the energy resolution to the hard X-ray region, beyond 3 keV and up to 79 keV. Before NuSTAR, other instruments, such as shadow cameras, operating in this energy range were used. However, these were not true focusing telescopes; they relied on indirect methods like coded aperture masks for image reconstruction, which limited their spatial resolution and sensitivity compared to the direct focusing capabilities of NuSTAR. The NuSTAR detailed design phase began in 2008, and it was launched to a near-equatorial low-Earth orbit in 2012 [5]. Each of the two NuSTAR optics modules is comprised of 133 layered shells coated with multilayers of different materials (Pt/C inner shells, W/Si for outer shells), and uses a segmented glass technology approach. From layers 1 to 69, the mirror shells are divided into 6 sextants, and from layers

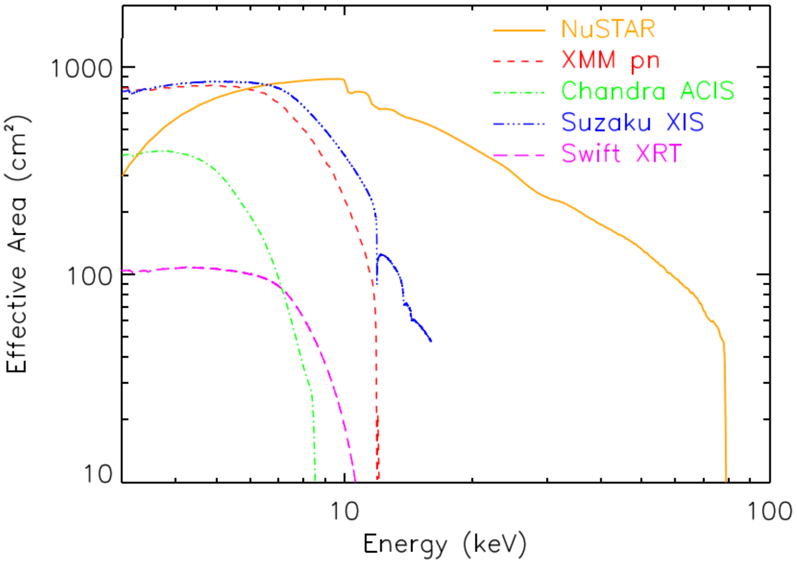

Figure 3: The effective collecting area of NuSTAR is compared to that of other X-ray telescopes, Swift, Chandra, XMM, and Suzaku. From [5].

69 to 133, they are further divided into 12. This segmented technology is essential to reduce the overall weight of the optics. However, this segmentation comes with a trade-off, it slightly decreases the angular resolution compared to a single-piece mirror. The shells are arranged in a conical shape that approximates a Wolter-I geometry, designed for grazing-incidence reflection. These optics are designed to focus X-rays onto two separate solid-state detectors positioned in the focal planes, which are located approximately 10 meters away from the optics themselves. The telescopes and detectors are intentionally designed to be nearly identical, enabling their focal plane images to be merged to enhance sensitivity. The focal plane is made up of a 2 by 2 array of CdZnTe (Cadmium Zinc Telluride) pixel detectors, each containing a grid of 32 by 32 pixels, where each pixel measures 0.6 mm, resulting in a FOV of 12” in x and y.

Figure 3 presents the effective area of NuSTAR as a function of energy, in comparison with other X-ray missions. The use of low grazing angle X-ray optics combined with multilayer coatings, allows NuSTAR to collect significant amounts of X-rays up to 78.4 keV, where the Platinum K absorption edge is located. The observatory’s angular resolution, primarily determined by its optics, stands at 18” FWHM (Full Width at Half Maximum), with a half-power diameter of 58”. Designed for effective performance in the hard X-ray spectrum, NuSTAR’s focal plane achieves an energy resolution, with a FWHM response of 400 eV at 10 keV and 0.9 keV at 60 keV. On the other hand, the calibrated NuSTAR event timestamps for a typical observation are shown to be accurate to a precision of $\sim 65\mu$s [30].

NuSTAR’s sensitivity to the high-energy spectrum will allow us to accurately identify and analyze the characteristic power-law component(s) typical of magnetars. Additionally, the light-curves obtained from NuSTAR will enable us to detect and analyze the characteristic periodicity of a few seconds that is typical of magnetars.

3.3 Neil Gehrels Swift Observatory (Swift)

Launched on November 20, 2004 by NASA, the *Swift Gamma-Ray Burst Mission*, [4], commonly known as Swift, is a multi-wavelength space observatory designed to study gamma-ray bursts

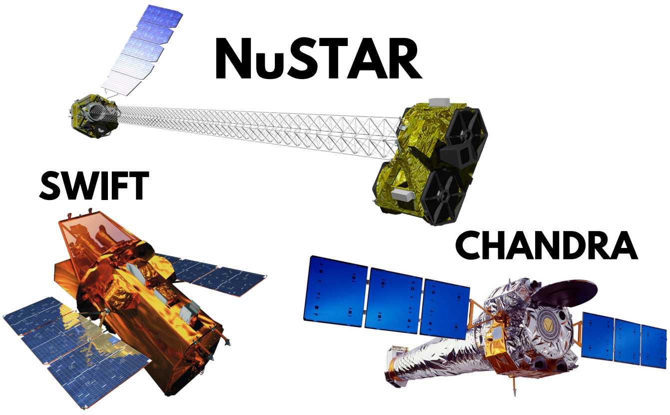

Figure 4: Depiction of the NuSTAR (top), Swift (left) and Chandra (right) X-ray observatories.

(GRBs) and other high-energy astronomical phenomena. The mission is a collaborative effort involving NASA, the United Kingdom Space Agency (UKSA), and the Italian Space Agency (ASI). Swift's primary objectives are to detect and observe GRBs in the gamma-ray, X-ray, ultraviolet (UV), and optical wavelengths, providing rapid and precise localization of these events to facilitate follow-up observations. The X-Ray Telescope (XRT) aboard Swift is a crucial instrument for studying high-energy phenomena. It is designed to quickly and accurately localize X-ray sources and monitor their temporal and spectral evolution. It uses a grazing-incidence Wolter I telescope to focus X-rays onto a CCD. It does not, however, use any multilayer-coated mirrors like NuSTAR and is thus limited to energies between 0.2 and 10 keV. The XRT's optics consist of single-layer gold-coated mirrors fabricated as replicated shells (as opposed to NuSTAR's segemented technology), which helps to improve angular resolution, 18" half-power diameter at 1.5 keV. Its effective area as a function of the energy can be seen in Figure 3.

The better resolution in the low energy part will allow us to improve our information about the N_H, the hydrogen column density, which is a measure of the number of hydrogen atoms along a line of sight between an observer and a particular astronomical source. It will also help us to improve the black body parameters.

3.4 Chandra X-ray Observatory (CXO or Chandra)

The Chandra X-ray Observatory is one of NASA's Great Observatories, a series of four advanced space telescopes launched to observe the Universe in different wavelengths of light [3]. Chandra was launched on July 23, 1999, aboard the Space Shuttle Columbia (STS-93).

Chandra's mirrors are the smoothest ever constructed, allowing it to produce images with unprecedented angular resolution. The four pairs of mirrors are designed in the Wolter Type I configuration (see Figure 2). They are crafted from high-grade, super-polished Zerodur glass, chosen for its low thermal expansion properties. The surface roughness of this polished glass is of the order of a few angstroms, which is crucial for achieving Chandra's exceptional angular resolution. With a resolution of 0.5 arcseconds, Chandra boasts the best angular resolution among X-ray telescopes, more than a factor 10 better than NuSTAR's 60 arcseconds.

The mirrors are coated with a thin layer of iridium, which provides high X-ray reflectivity in the energy range from 0.1 to 10 keV. Chandra includes different instruments, however, the data we analyze during this study is from the *Advanced CCD Imaging Spectromete* ACIS-S. The

ACIS-S instrument has an energy resolution of approximately 95 eV at 1.49 keV and 150 eV at 5.9 keV The collecting area of Chandra is shown in Figure 3.

Chandra's 0.5 arcsecond angular resolution will enable us to distinguish the magnetar SGR J1745-29 from SgrA* and other sources in the galactic center, allowing us to conduct an 11-year study of the magnetar's spectral properties.

4 Methodology of Data Processing and Analysis

Most observational X-ray data acquired by NASA missions is publicly available. The exception are datasets that have not yet undergone quality control and/or are proprietary for a certain period after the observation before becoming available to the scientific community in NASA's data archive aka the High Energy Astrophysics Science Archive Research Center (HEASARC). All data can be searched for using the HEASARC catalogue. While data come preprocessed shortly after the respective observation, it is highly recommended to reprocess all data with the latest software versions and calibration libraries before extracting science results to assure the most accurate conclusions. In order to process data, one needs the calibration files for the missions. Those are stored in the CALDB(Calibration Database), a specialized component within the HEASARC framework. These files are essential for converting raw data into scientifically usable formats by correcting for instrument-specific effects and ensuring the accuracy of the derived results.

NASA also provides the software tools necessary to process and analyse the raw data downloaded from the catalogue. HEASOFT (High Energy Astrophysics Software) is a comprehensive suite of software tools designed for the analysis of data from high-energy astrophysics missions. It includes mission-specific tools like the ones for NuSTAR, Swift and Chandra, tools to manipulate FITS files (FTOOLS) and high-level, multi-mission tasks for X-ray astronomical spectral, timing, and imaging data analysis (XANADU). During this project, we are using the HEASOFT version 6.32.1 . Next, we discuss the most relevant packages within the HEASOFT software utilized for the development of this project.

4.1 Raw Data Processing for NuSTAR, Swift and Chandra

4.1.1 NuSTAR Data Processing

In order to analyse the raw data (level 0) of the observation, the standard NuSTAR procedure was followed. First the data was reprocessed using the NuSTAR Data Analysis Software NUSTARDAS version 2.1.2 and NuSTAR CALDB version 20220510, following Analysis Quickstart Guide and the more detailed NuSTARDAS documentation. The NuSTAR data processing is organized into three stages:

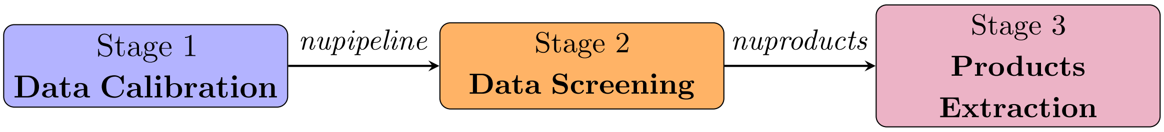

The first stage involves raw event files downloaded from the archive and calibration files, including altitude correction, orbital correction, bad pixels, gain correction, and others. There are specific functions for applying each of the calibrations to the events file. However, *nupipeline* can be used to automatically apply all standard calibrations, which is the approach we followed. After running *nupipeline*, the resulting files, known as 'Stage 2' files, are calibrated and cleaned event files ready for scientific analysis. But what exactly is an event file? Event files are FITS files that contain a header with information about the file and the observation, an event table with the main cleaned and calibrated event data (such as the energy, position, and time of each X-ray photon), Good Time Intervals (GTIs) indicating periods when the data are valid and free from significant instrumental or environmental interference, quality flags indicating the observation's quality, and exposure information detailing the duration and conditions of the observation. The extraction of high-level scientific products (Stage 3 files) can be accomplished in two ways. The general method for all NASA observatories involves using HEASOFT's *xselect* tool, a versatile and interactive command-line utility for data selection, filtering, and extraction (Detailed instructions on using *xselect* can be found in xselect user's guide). Alternatively, for NuSTAR data, the *nuproducts* tool can be used on the Stage 2 cleaned event files, which automatically invokes *xselect* scripts to perform the extraction of spectrum, light curves, sky images and ARF[d]/RMF[e] response files. In this project, we utilize the *xselect* tool for combining and filtering event files for the time analysis phase. Subsequently, we employ the *nuproducts* tool for the spectral analysis.

Both approaches, whether using the *xselect* tool or *nuproducts*, require spatial filtering. Filtering involves constraining the events to a specific region in the field of view, which will then be used for the extraction of scientific products. We use DS9, an astronomical imaging and data visualization software fully developed by the Chandra X-ray Center, to perform this task. DS9 is open source and widely used by the astronomy community for quick viewing and analyzing images of the sky from telescopes, both in optical and non-optical wavelengths [31]. Using DS9, we create the source, centered at the source, and background regions, typically circular or annulus shapes for our case (See Figure 5 as an example).

The NuSTAR background at lower energies ($E < 20$ keV) is primarily dominated by the cosmic X-ray background (CXB). At higher energies, the background can arise from various phenomena, such as stray light from sources outside the field of view (FoV), solar X-rays during flares that penetrate the spacecraft, and gamma rays hitting the spacecraft, which produce bremsstrahlung or continuum emission. Each focal plane modules (FPM) comprises four different chips, each with its own intrinsic detector background. When selecting the optimal region for background extraction, ideally, the background region should be placed on the same CCD chip as the source while avoiding any evident contamination, such as straylight.

It's important to mention that NuSTAR has two similar detection lines with both optics focusing onto two similar but separate focal plane modules (FPM) aka two detectors referred to as FPMA and FPMB[f], respectively. The data from each telescope is analyzed independently during all stages. Then it will be merged together, during the scientific analysis (e.g. spectral or timing analysis).

We will use NuSTAR data to perform spectral analysis of the magnetar SGR J1745-29 during its outburst in 2013 and the subsequent years. Additionally, we will utilize NuSTAR data from

---

[d] ARF (Auxiliary Response File): describes the effective area of the X-ray telescope as a function of energy, taking into account the detector's efficiency, the telescope's mirror area, and any filters.

[e] RMF (Response Matrix File): describes the energy resolution and the probability distribution of the detected photon energies.

[f] The files corresponding to the FPMA instrument are labeled with A *nu100A01_cl.evt*, those for the FPMB with B, respectively,*nu100B01_cl.evt*.

the same object during the outburst to conduct timing analysis.

4.1.2 Swift Data Processing

In the same way as NuSTAR, HEASOFT includes a package for analyzing Swift data, specifically for the XRT experiment. The version 0.13.7 of *xrtpipeline* was used for this project, as described in XRT Data Analysis and the Swift XRT Data Reduction Guide, to extract the required science data. Applying the *xrtpipeline* to the the Stage 1 data, will produce cleaned and calibrated events file (Stage 2). Unlike NuSTARDAS, no automated pipeline exists for extracting the high level scientific products (Stage 3), like spectra and light curves, such that the *xselect* package must be used to manually extract them. In the same way as in the NuSTAR data analysis, we must create regions for the source and background. The response files for the instrument, such as Auxiliary Response Files (ARFs) and Response Matrix Files (RMF) must be created using *xrtmkarf*, a dedicated tool that builds the ARFs by using instrument exposure maps (files that correct features like vignetting effects or detector issues) generated in the Stage 2.

Swift data will be used in conjunction with NuSTAR to perform a joint analysis of the SGR J1745-29 spectrum during its outburst.

4.1.3 Chandra Data Processing

Unlike NuSTAR and Swift, CIAO (Chandra Interactive Analysis of Observations) is not part of the HEASOFT, is a software package developed by the Chandra X-ray Center (CXC) for analyzing data from the Chandra X-ray Observatory. However, Chandra's event data is also stored in the HEASARC archive, and the calibration files in CALDB. As we mentioned, one needs to install CIAO (independently of the other software) from the CIAO web page. For this project, we installed CIAO Version 4.16.0 and CIAO CALDB 4.11.0, and followed the Chandra Data Analysis tutorial and the User's Guide.

After downloading the raw event data from the HEASARC archive, we used CIAO's *chandra_repro* to produce the Stage 2 event files. Similar to NuSTAR and Swift, both source and background regions were created using DS9. We then utilized CIAO's *specextract* to extract the Stage 3 scientific files, including spectra, light curves, and response files.

Chandra data will be utilized to analyze the soft X-ray spectrum of SGR J1745-29 using observational data spanning 11 years.

4.2 Scientific Data Analysis with XSPEC and HENDRICS

4.2.1 Spectral Analysis Using XSPEC

XSPEC (X-ray Spectral Fitting Package) is a software tool for X-ray astronomy toanalyse spectral features of cosmic X-ray sources [32]. Developed and maintained by NASA's HEASARC, XSPEC provides a powerful and flexible platform for fitting models to observed X-ray data and extracting physical parameters, while providing the ease of taking care of several mission specific features automatically. The XSPEC Users' Guide Version 12.13.1 can be followed. XSPEC is designed to fit theoretical models to observed X-ray spectra. This involves adjusting model parameters to minimize the difference between the observed data and the model predictions, typically using statistical methods like chi-squared minimization or maximum likelihood. It also includes a library of predefined spectral models, which can describe a wide range of astrophysical processes and sources. In addition, XSPEC is capable of including instrument response files (ARF/RMF).

The workflow in XSPEC involves several key steps. First, users load their observational data, typically in the form of .pha files, along with the corresponding response files (.arf and .rmf) into XSPEC. Next, a spectral model is defined by combining multiplicative models (e.g., TBabs for absorption) and/or additive models (e.g., BBody for blackbody radiation) from the extensive XSPEC model library. After specifying the initial parameters for the model, the data is fitted to the model to determine the best-fitting parameters and to analyze the underlying physical processes of the observed X-ray source. XSPEC also allows to specify a .pha[g] file as the background for the data, enabling background subtraction during the analysis. This feature will be utilized in subsequent stages of our analysis to ensure accurate results by accounting for and removing the background noise from the observed data.

XSPEC's fitting tool uses various algorithms to perform the data fitting, the most common being the Levenberg-Marquardt algorithm. The fitting process includes several steps. Initially, XSPEC computes the theoretical spectrum using the specified model and initial parameters. It then calculates the residuals, or differences between the observed data and the model, using the chi-square (χ^2) statistic (Gaussian-distributed data), although other statistics like the C-statistic (Poisson-distributed data) can also be employed. The fitting algorithm adjusts the model parameters to minimize the expression:

$$\chi^2 = \sum_i \frac{(D_i - M_i)^2}{\sigma_i^2} \tag{8}$$

where D_i are the observed data points, M_i the model predictions and σ_i the uncertainties in the data points. Finally, this process iterates until the parameters converge to a χ^2 value. The goodness-of-fit is evaluated using the reduced chi-square value $\chi^2_{red} = \chi^2/dof$, where dof are the degrees of freedom, and a value close to 1 will indicate a good fit. XSPEC's *error* function computes parameter errors by varying the parameters until the value of the fit statistic is equal to the last value of the fit plus $\Delta\chi^2 = 2.706$, which is equivalent to the 90% confidence level for a single parameter.

Below, we will describe the models used for spectral fitting in the presented analysis as detailed in Section 5:

1. **TBabs (Tübingen-Boulder ISM Absorption Model):** The `TBabs` model accounts for the interstellar absorption by neutral gas. The transmission factor $T(E)$ for a photon of energy E is given by:

   $$T(E) = \exp\left(-N_H \sigma(E)\right), \tag{9}$$

   where N_H is the equivalent hydrogen column density in units of atoms cm^{-2} and $\sigma(E)$ is the photoelectric cross-section per hydrogen atom (dependent on energy and the elemental abundances).

2. **BBody (Blackbody Radiation):** The `BBody` component models the thermal emission from a hot, optically thick plasma, which is described by Planck's law. The spectral

---

[g] A .pha file is a type of FITS (Flexible Image Transport System) file used primarily in high-energy astrophysics, such as X-ray and gamma-ray astronomy. The .pha extension stands for 'PHA', which is short for 'Pulse Height Amplitude'.

radiance $I(E)$ of a blackbody is given by:

$$I(E) = \frac{8\pi h E^3}{c^3} \frac{1}{\exp(E/kT) - 1}, \tag{10}$$

where h is the Planck constant, c is the speed of light, k is the Boltzmann constant, T is the temperature of the blackbody, and E is the photon energy.

3. **Power (Power-law model):** The `Power` component represents non-thermal processes such as synchrotron radiation or inverse Compton scattering. The power-law model is given by:

$$I(E) = KE^{-\Gamma}, \tag{11}$$

where K is the normalization constant and Γ is the photon index that describes the slope of the spectrum.

4. **BknPower (Broken Power-law model):** The `BknPower` component models spectra that exhibit different power-law behaviors at low and high energies, typically due to a break in the physical process generating the emission. The broken power-law model is given by:

$$I(E) = \begin{cases} KE^{-\Gamma_1} & \text{for } E \leq E_{\text{break}}, \\ KE_{\text{break}}^{\Gamma_2 - \Gamma_1} E^{-\Gamma_2} & \text{for } E > E_{\text{break}}, \end{cases} \tag{12}$$

where K is the normalization constant, Γ_1 and Γ_2 are the photon indices before and after the break energy E_{break}, respectively.

5. **Gauss (Gaussian Line):** The `Gauss` component models emission lines, such as those from ionized elements in the plasma. The Gaussian profile is given by:

$$I(E) = \frac{A}{\sqrt{2\pi\sigma^2}} \exp\left(-\frac{(E - E_0)^2}{2\sigma^2}\right), \tag{13}$$

where A is the total flux of the line, E_0 is its centroid energy, and σ is the standard deviation.

We will use XSPEC to perform spectral fitting of the NuSTAR, Swift, and Chandra observations to the aforementioned models.

4.2.2 Timing Analysis Using HENDRICS

HENDRICS (High Energy Data Reduction Interface from the Command Shell) is a Python package designed for spectral-timing analysis of X-ray astronomical data. It was originally developed under the name MaLTPyNT by Matteo Bachetti [33] to handle timing analysis for NuSTAR data, addressing issues related to the long dead times and orbital gaps typical of this mission's data. HENDRICS extends MaLTPyNT capabilities, offering tools for power density and cross spectra, time lags, pulsar searches, color-color, and color-intensity diagrams.

The development of HENDRICS was motivated by the need to provide efficient and accurate spectral-timing analysis, leveraging the core functionalities of the Stingray package. Stingray itself is a comprehensive spectral-timing software suite, affiliated with the Astropy project, and developed collaboratively by a community of X-ray astronomers and software developers. The HENDRICS package allows for quick analysis and can handle data from multiple X-ray satellites, like NuSTAR, Swift and Chandra.

We will use HENDRICS *HENzsearch* to perform a Z_3^2 analysis over a range of trials frequencies for the NuSTAR 2013 SGR J1745-29 data.

During the course of this project, an X-ray timing analysis software package, XTimeAnalysis, was developed based on the H-test (see Appendix D for a review of the H-test algorithm). However, after applying it to the 2013 data for SGR J1745-29, the precision obtained for the period was inconsistent in the third decimal place compared to the results obtained by Kaspi et al. (2014) (3.760 s vs. 3.763 s obtained by Kaspi et al. and using HENDRICS). This discrepancy was likely due to the lack of an algorithm capable of handling telescope deadtimes, thus. Thus, we decided to use HENDRICS, which an open source tool that has been developed by the comunity of experts in the field of X-ray timing analysis.

5 Results and Discussion

SGR J1745-29 is a magnetar situated in the Galactic Center, gravitationally bound to the Milky Way's supermassive black hole, Sgr A*. This intriguing object was discovered in April 2013 by both the Swift X-ray Observatory [6] and the NuSTAR Observatory [7]. The identification of SGR J1745-29 as a magnetar was based on several distinguishing features, including magnetar-like bursts, periodicity, and its spectral characteristics. Chandra's follow-up localized the pulsar to be 3" away from the Sgr A* position, determining the magnetar's coordinates as $\alpha = 17^{\mathrm{h}}45^{\mathrm{m}}40^{\mathrm{s}}21,\ \delta = -29^{\circ}00'29''2$, with an uncertainty of 1".9 (radius, 90% confidence)

This section is structured as follows: First, in Subsection 5.1, we reproduce the Swift and NuSTAR spectrum results from Ref. [7] to ensure the reliability of our procedure. Subsequently, in Subsection 5.3, we conduct a hard X-ray spectral study using NuSTAR data over two years following the outburst. Next, in Subsection 5.2, we perform a soft X-ray analysis over an 11-year period, up to the 2023 Chandra observations, to investigate a potential hint identified by the TFG [10]. Finally, in Subsection 5.4, we replicate the timing analysis results from Ref. [8] and look at a additional data set.

5.1 Initial Observations of SGR J1745-29 by Swift and NuSTAR

To ensure reliable results, we will use the NuSTAR discovery paper on SGR J1745-29 [7] as a baseline for our analysis and verify all software and its use against these published results. The abovementioned discovery paper for SGR J1745-29 uses two NuSTAR observations and five Swift observations conducted between April and May of 2013. Among the five Swift observations mentioned, only two (IDs 00035650242 and 00554491001) were available in the HEASARC archive. The NuSTAR observations used in the presented analysis are identical to those in [7], i.e. we used IDs 30001002006 and 80002013002 (specific information about the observations like date or exposure times are in Table C1 of the Appendix).

As outlined in Section 4.1.1, we used the NuSTARDAS software to process the data and extract spectra. In case of the data analysis of SGR J1745-29, the source region was determined as the same 1' region used in Ref. [7], centered at the Chandra coordinates specified at the beginning of this section. To follow the same procedure as Ref. [7], we used observation ID

30001002003 from 2012 to provide a reference background. This approach accounts for the strong diffuse emission and the numerous unresolved sources by NuSTAR within the Sgr A complex. The observation was taken when the magnetar was inactive and Sgr A* did not exhibit any detectable flares. We subtracted exactly the same 1' region as used as the source region for the outburst observation. This background definition allows us to account for the strong diffuse emission and unresolved sources within Sgr A*. All spectra obtained was rebinned with a bin size chosen to include at least 30 counts per bin.

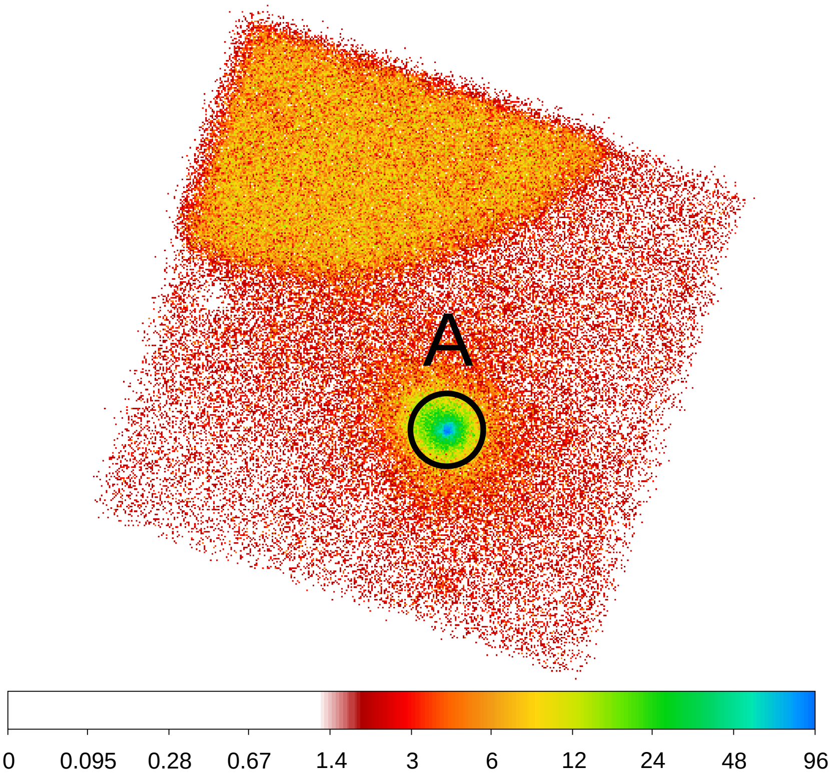

Figure 5: FOV $12' \times 12'$ of the NuSTAR observation ID 30001002006, which shows the number of counts detected during the observation for each pixel in a given energy range (3-78 keV). Region A corresponds to the 1' NuSTAR source region used by [7]. The circle covering the upper left corner corresponds to contamination from a source outside the FoV (called "ghostrays").

Incorporating Swift data enhances our sensitivity in the low energy range, covering 1.5 to 7 keV and providing overlap with the NuSTAR data from $1.5-3$ keV. We used the Swift XRT Data Analysis software to process and prepare these observational data (as discussed in Subsec. 4.1.2). The same regions defined by [7] for the Swift data were employed, with a 22" region for the source and an annular region with inner and outer radii of 70" and 160", respectively, for the background as shown in Fig. 6. Both, circular and annulus are centered at the Chandra reference coordinates.

NuSTAR and Swift spectral data were jointly analyzed using the XSPEC software. We used two models, each being a combination of different XSPEC submodels (detailed info about the models in Section 4.2.1). The first one is `TBabs x (BBody + Power + Gauss)`, the multiplicative model for absortion TBabs, and additive models for a blackbody, power law and a Gaussian line feature description. Compared to the study by Ref. [7], we included an additional Gaussian component to better fit the 6.6 keV Fe Kα emission, attributed to the high abundance of iron in

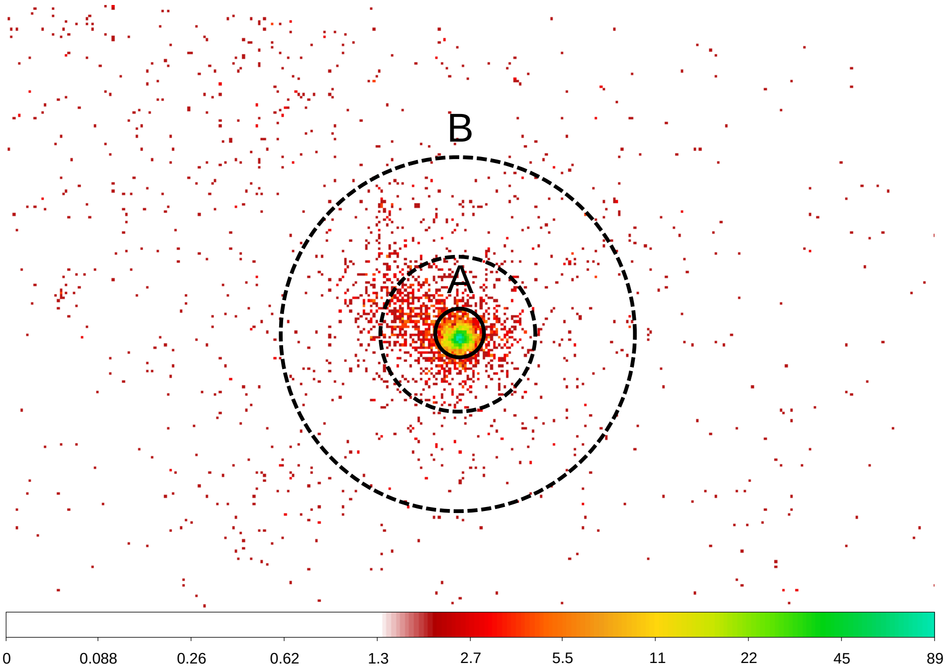

Figure 6: A zoomed-in view of the FOV ($23.6' \times 23.6'$) of one of the Swift observation ID 00554491001. Region A corresponds to the 22" source region used by [7]. The 70" and 160" background annulus region is also shown as B.

the galactic center. Additionally, we also use a broken power law replacing the initial standard power law `TBabs x (BBody + BknPower + Gauss)`, which typically results in a better fit to the hard X-rays present in several magnetars (e.g. Ref. [34]). On the other hand, we constrained the energy range from 1.5 to 30 keV since the source was not detected at higher energies in any observation, according to the follow up study by Ref. [8].

The parameters of the best-fit results are summarized in Table 1, and the fitted spectrum is shown in Figure 7. With the shown parameters for the fitting models, we obtain for the simple power law a reduced χ^2 of $\chi^2_{\rm red} = \chi^2/d.o.f = 1.18$, and for the broken power-law model a $\chi^2_{\rm red} = 1.04$, which indicates that the broken power-law describes our data slightly better, since it is closer to one. We obtained that:

- **The broken power-law model** fit values for $kT = 0.90^{+0.04}_{-0.04}$ keV and $N_H = 11.7^{+1.0}_{-0.8} \times 10^{22}\text{cm}^{-2}$ are slightly lower than the ones obtained by Ref. [7] [h]. However, the N_H and kT obtained using Chandra data by [35] shows that N_H and kT may be lower than in [7] ($N_H = 10.1$ and $kT = 0.88$). Since both parameters are dominant in the soft energy band, for which Chandra is better, we can determine that our results are reliable. On the other hand $\Gamma_1 = 3.5(1)$ and $\Gamma_2 = 2.2$ are in agreement with the typical values obtained for other magnetars (See Subsec. 2.4).
- **For the simple power law** we obtained a much lower $N_H = 8.7(5)$ but the same $kT = 0.90(2)$ keV as for the broken power-law case. Finally, the simple photon index obtained is $\Gamma = 2.6(1)$, which differs from Ref. [7].

We can conclude that our results are in agreement with typical values of magnetars for the non-thermal hard X-ray spectrum, a broken power-law being a good fit. For the soft X-ray

---

[h] Values obtained by authors of Ref. [7] are in Table 1

Table 1: Best fit values for the initial observations of SGR J1745-29 by Swift and NuSTAR

Data[a]	E (keV)	Fit Model[b]	N_H[c] ($\times 10^{22}$ cm^{-2})	kT[d] (keV)[d]	Γ_1/Γ [e]	E_{bk}[f] (keV)	Γ_2	Flux[g]	χ^2_{red}
S/N	1.5–30.0	BB+BPL+G	$11.7^{+1.0}_{-0.8}$	$0.90^{+0.04}_{-0.04}$	$3.5^{+0.1}_{-0.1}$	$12.5^{+0.5}_{-0.5}$	$2.2^{+0.1}_{-0.1}$	$1.9^{+0.02}_{-0.04}(12)$	1.02
S/N	1.5–30.0	BB+PL+G	$8.7^{+0.5}_{-0.4}$	$0.90^{+0.02}_{-0.01}$	$2.6^{+0.1}_{-0.1}$	...	...	$4.64(12)^{+0.05}_{-0.03}$	1.19
S/N	1.5–30.0	BB	$4.5^{+0.1}_{-0.1}$	$1.2^{+0.02}_{-0.01}$	...	...	...	$3.61^{+0.03}_{-0.03}(11)$	6.94
[7]	1.7–79	BB + PL	$14.20^{+0.71}_{-0.65}$	$0.956^{+0.015}_{-0.017}$	$1.47^{+0.46}_{-0.37}$	...	...	$6.22 \pm 0.57(12)$	1.01

[a] S/N means Swift and NuSTAR.

[b] BB means blackbody, BPL means broke power-law, PL power-law and G gaussian. For all the cases we are multiplying by the TBabs absorption model.

[c] Absorbed column density.

[d] Blackbody temperature.

[e] For the broken power law it corresponds to Γ_1 and for the simple to Γ.

[f] Energy break for the broken power law model.

[g] Flux for the entire energy range. Units are ergs/cm^2/s $\times 10^{-X}$, where X is the number inside the parenthesis.

energy band even though they are slightly different than the ones obtained by the discovery paper [7], they agree with Chandra studies, which are more precise in the soft energy band.

We note that the reduced χ^2 obtained by Ref. [7] for the simple power law is slightly better than our value for the same model. One possible explanation may be that we only used two Swift observations in our analysis, instead of the five that were previously used. Since Swift data helps especially with constraining N_H due to its lower energy threshold, we would expect an improved overall fit. Unfortunately, the additional 3 Swift observations were not available on the public archive.

Either way, our fit results are in agreement with having a non-thermal component for the higher energy range present, as indicated by a larger reduced χ^2 of $\chi^2_{\mathrm{red}} = 6.94$.

5.2 Longterm Monitoring of SGR J1745-29 with Chandra

SGR J1745-29 stands out as the magnetar with an extensive observational data covering over the last 10 years. This is due to its proximity to SgrA*, which is a crucial region of interest for X-ray studies and is therefore continuous monitored and studied in detail by the scientific community. Leveraging these accumulated observations, we conducted a comprehensive temporal evolution analysis of its soft X-ray spectral parameters, especially N_H, kT and a flux estimation based on the normalization factor of the blackbody. To achieve this, we will utilize data from the Chandra X-ray telescope for each year from 2012 to 2023. (Details about the observation can be found in Table C1). As we mentioned in Section 3, Chandra's subarcsec angular resolution will allow us to resolve SGR J1745-29 from SgrA*, which is just a few arcseconds apart.

We will adopt the same methodology as the 3.5-year follow-up study previously conducted by Ref. [9], and restrict the energy range to $0.3 - 8$ keV. As fit model we are utilizing an absorbed blackbody model `TBabs(Bbody)` only, since we do not expect the power law component to have a significant impact at these energies. The processing of the data was done with Chandra's processing software CIAO following what is detailed in Section 4.1.3. Similarly to work in Ref. [9], a 1.5" region centered on the exact Chandra coordinates was used as a source. The FoV of the

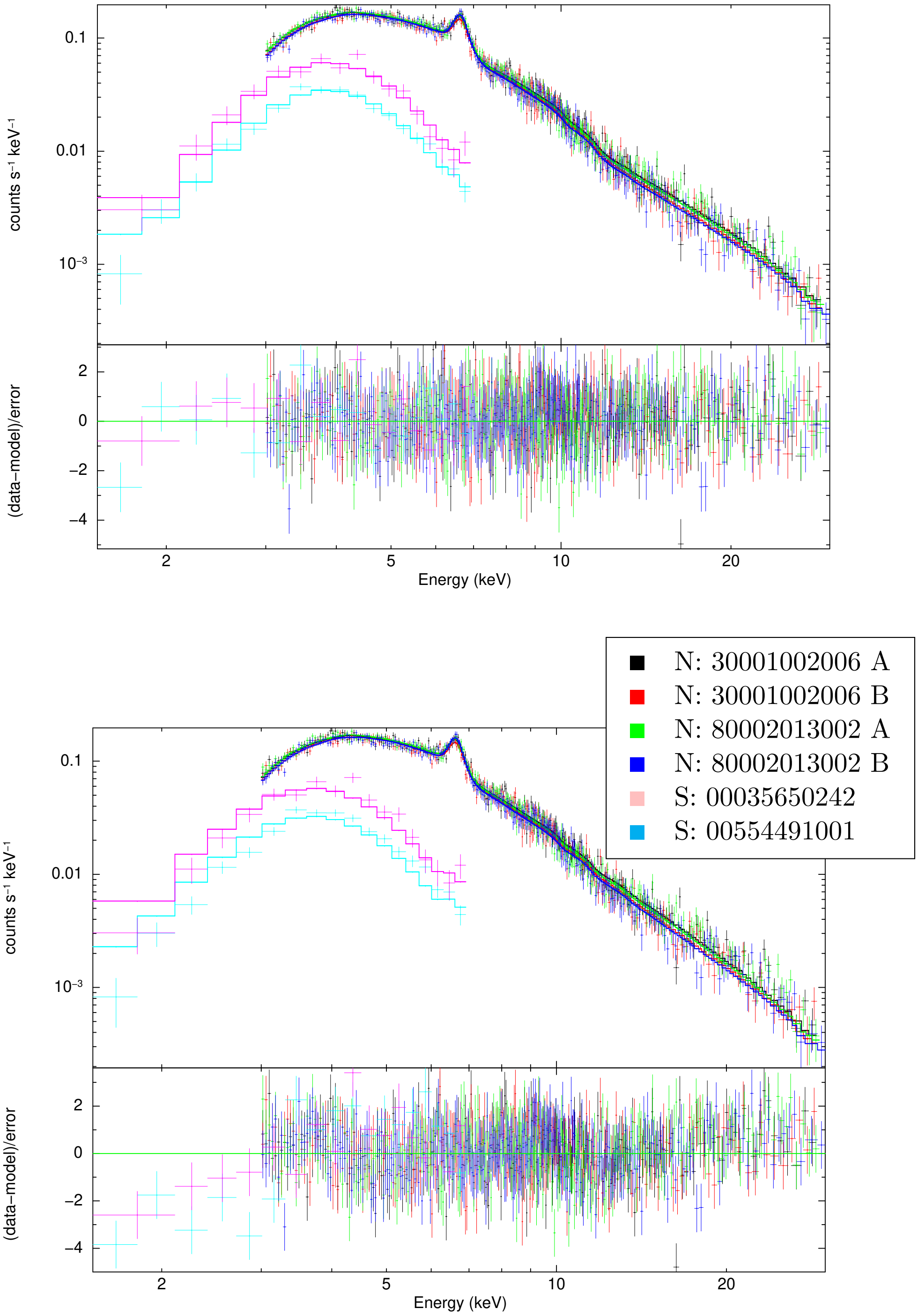

Figure 7: Spectral data for the 2013 SGR J1745-29 observations with different fitting models. The top (bottom) plot shows data for NuSTAR (N) and Swift (S) fitted with a broken powerlaw (simple power law), respectively. Within each main plot, the top part displays the data (+) and the best fit (solid line), while the bottom plot indicates the goodness of fit. The legend provides the ObsIDs.

observation ID 15043 is shown, in Figure 8 (where one can clearly distinguish our magnetar and SgrA* right outside region A). For comparison, a 22" region (B) is shown corresponding to the Swift angular resolution (the NuSTAR source region is even bigger), which is clearly not able to resolve the two sources seperately. In the study of Ref. [9], the background was estimated for each observation. Since the authors do not provide any more information about the background regions, we opted to use a 22" circular region centered approximately 25" below Sgr A*, C in Figure 8.

The spectral fitting was performed using the same XSPEC fitting tools and routines verified against the initial SGR J1745-29 data (Sec. 5.1). The observational data was analyzed using two approaches: first, by fitting all the observations with all parameters left free to vary, and second, by fixing $N_H = 11.3\text{cm}^{-2} \times 10^{22}$, for the lower statistics observations. $N_H = 11.3$ corresponds to the best fit value for the outburst year 2013, and is also consistent with our 2015-16 best fit. The second approach was used because leaving N_H as a free parameter resulted in a substantial decrease in the value of N_H (See top panel of Figure 9), which is not feasible given that the equivalent hydrogen column density is generally stable over timescales of years. The poor constraint of N_H by the fits is most likely caused by low statistic when the magnetar slowly enters its quiescent phase after outburst, so freezing this parameter will improve our results for the blackbody fits and their kT values. Therefore we continue the analysis with the fixed NH value. The best-fit parameters are shown in Table 2. Figure 9 summarizes the evolution of the selected fit parameters with time over the considered time period from 2012 to 2023 for N_H free (black) and frozen to the literature value (red) during data model fitting.

The following tendencies, can be observed:

- **The hydrogen column density** N_h is fixed to the best value for 2013, 2015 and 2016 $N_H = 11.3 \times 10^{22}\text{cm}^{-2}$. As indicated by the black dots in the top panel or Figure 9, NH would otherwise vary against expectations, potentially degrading other fit components.

- **The blackbody temperature** kT is around 0.87 keV for the outburst year 2013, then it slowly decrease towards a pretty constant value of 0.7 which is maintained from 2016 to 2023. The temperature value for 2012 (preoutburst) and 2013 (outburst) agree within errors. This is unexpected, since the flux is two order of magnitude lower. Another possibility is that, due to low quiescent flux from the magnetar pre-outburst and its proximity to Sgr A*, the 1.5" region we are using is receiving flux from both sources, resulting in a combined kT of both blackbodies, and explaining the poor fit $\chi^2_{red} = 1.86$

- **The model flux** increases substantially in outburst $6 \times 10^{-12}\text{ergs/cm}^2\text{s}$ and then it decrease steadily to the $10^{-14}\text{ergs/cm}^2\text{s}$ value for the quiescent years.

Our results are consistent with those obtained by [9], where the temperature and fluxes decreased in the years following the outburst. Their last recorded value for the end of 2014 was $kT = 0.77$ keV, which aligns with our measurement of $kT = 0.80 \pm 0.03$ keV for the year 2015. According to our results, the kT seems to get a bit lower for the following years, stabilising at around ~ 0.7 keV.

This result, rules out the possible hint found by the TFG [10], where a possible increase in the kT to 1.2 keV using a 2022 NuSTAR observation was found. Since Chandra is more sensitive to the blackbody temperature, our results for 2022 of $kT = 0.74^{+0.13}_{-0.10}$ keV rules out the hint.

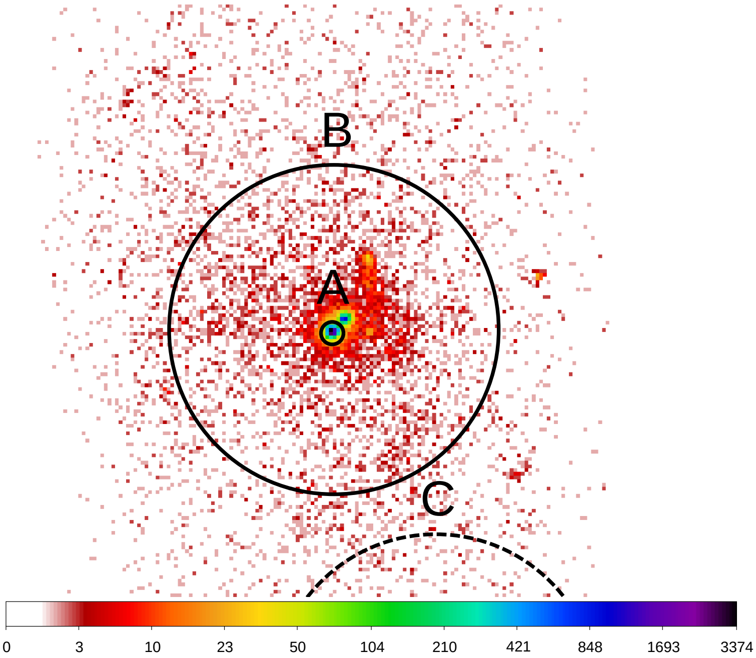

Figure 8: A zoomed-in view of the 2013 Chandra observation (ID 15043). The total FOV in ACIS mode would be ($16.9' \times 16.9'$). Region A corresponds to the 1.5" source region, i.e SGR J1745-29. The bright spot to the top right of the magnetar corresponds to the location of Sgr A*. A 22" region corresponding to the Swift source region (Region B) is also displayed for illustration of the angular resolution capabilities of both instruments. It is evident that we cannot resolve SGR J1745-29 from Sgr A* with X-ray observatories other than Chandra. Lastly, region C (dashed), which is only partially shown, indicates the location of the 22" background region used in the Chandra analysis.

5.3 The Hard X-Ray Spectrum of SGR J1745-29

NuSTAR observations enable us to examine the hard X-ray energy range of the magnetar's spectrum, specifically above 10 keV, a region inaccessible to any other telescope. We performed a study on this energy range using four NuSTAR observations from 2013, 2014 and 2015, with IDs 30001002006, 80002013026, 30002002002, and 30002002008 (see Table C1). However, we found X-ray transients inside the 1' region source for all of them. Those were confirmed using Chandra observations (NuSTAR cannot spearate the magnetar from the transient). Hence, any attempt to produce spectral results with this data is affected by the transients flux, forcing us to abandon this study.

5.4 SGR J1745-29 Timing Analysis

Timing analysis is of significant importance for magentar studies, since the surface magnetic field can be determined from knowing the NSs period P together with its time derivative $\dot{P}$ (see first part of Eq. 1). As mentioned in Subsection 4.2.2, we are using the Python package HENDRICS to realize the timing analysis study. To this end, we combined two NuSTAR observations from April 2013 (ID 30001002006 and 8000201302) and merged them into a single file using *xselect*. From this combined file, a source region of 1' radius centered on the magnetar's Chandra coordinates was extracted. Using the HENDRICS function `HENzsearch` a Z_3^2 analysis was made (see Appendix D)

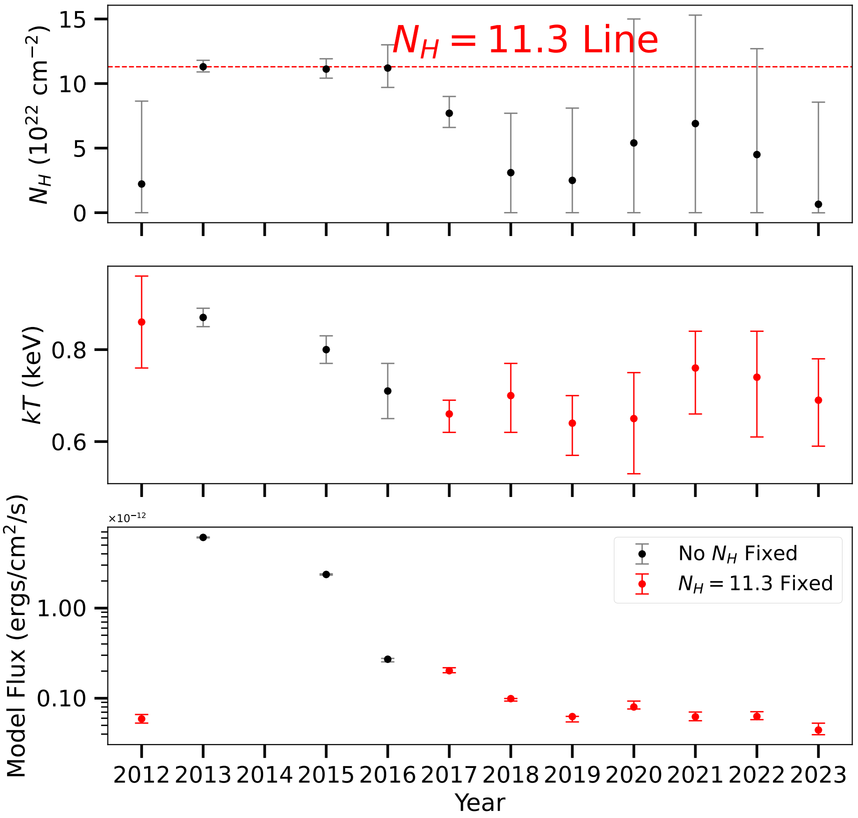

Figure 9: Temporal evolution of the spectral parameters for the blackbody model and the 0.3-8 keV absorbed flux of SGR 1745-2900 based on Chandra observations. Black dots represent the best fit values leaving N_H as a free parameter. Red dots represents the best fit values when one fixes the $N_H = 11.3$. This was only done for 2012, 2017, 2018, 2019, 2020, 2021, 2022 and 2023, since for the years 2013-15-16 the N_H is consistent with the 11.3 value therefore red and black dots are the same here.

between frequencies $f_{min} = 0.25$ Hz and $f_{max} = 30$ Hz. The best fit values obtained are listed in Table 3 labeled 'April 2013', the Z_3^2 power can be seen in the left part of Figure 10 and the phase profile in the left profile of Figure 11. The best period obtained $P = 3.763534(6)$ s differs by approximately 26μs from the value reported by [7][i], although their analysis was done using merged Swift and NuSTAR data. The best spin-down rate obtained is $\dot{P} = 2(2)\ \times 10^{-10}$, which implies a polar magnetic field of $B_p = 9(6)\ \times 10^{14}$ G.

Similarly, we aimed to replicate the findings from the NuSTAR follow-up study made by [8] shortly after the initial discovery of the magnetar. This study used a total of 12 NuSTAR and 9 Swift observations conducted in the period between April and August 2013. The observations were categorized into two groups: one spanning from April to the end of May, and the other from the end of May to mid-August. This division was based on the significant differences observed in the time of arrival of photons between the two ephemeris. In this study, we will exclusively use NuSTAR data covering the first ephemeris (IDs 30001002006, 80002013002, 80002013004,

---

[i] Period reported by Mori et al. $P = 3.7635603(68)$

Table 2: Best fit parameters for the soft X-ray Chandra analysis

Years	E (keV)	Fit Model[b]	N_H[c]($\times 10^{22}$ cm^{-2})	kT (keV)[d]	Flux[e]	$\chi^2_{\rm red}$
2012	0.3-8	BB	11.3	0.86 ± 0.10	$5.9^{+0.7}_{-0.7}(14)$	1.86
2013	0.3-8	BB	$11.3^{+0.5}_{-0.4}$	0.87 ± 0.02	$5.77^{+0.07}_{-0.07}(12)$	1.20
2015	0.3-8	BB	$11.1^{+0.7}_{-0.8}$	0.80 ± 0.03	$2.24^{+0.04}_{-0.04}(12)$	1.16
2016	0.3-8	BB	$11.2^{+1.8}_{-1.5}$	0.71 ± 0.06	$2.62^{+0.13}_{-0.13}(13)$	1.03
2017	0.3-8	BB	11.3	$0.66^{+0.04}_{-0.03}$	$2.02^{+0.10}_{-0.10}(13)$	1.53
2018	0.3-8	BB	11.3	$0.70^{+0.08}_{-0.07}$	$9.9^{+0.3}_{-0.3}(14)$	1.17
2019	0.3-8	BB	11.3	$0.64^{+0.07}_{-0.06}$	$6.26^{+0.03}_{-0.03}(14)$	1.46
2020	0.3-8	BB	11.3	$0.65^{+0.12}_{-0.10}$	$8.0^{+1.3}_{-1.3}(14)$	0.99
2021	0.3-8	BB	11.3	$0.76^{+0.10}_{-0.08}$	$6.2^{+0.8}_{-0.8}(14)$	0.81
2022	0.3-8	BB	11.3	$0.74^{+0.13}_{-0.10}$	$6.3^{+0.8}_{-0.8}(14)$	0.72
2023	0.3-8	BB	11.3	$0.69^{+0.10}_{-0.09}$	$4.4^{+0.8}_{-0.8}(14)$	0.82

[a] BB means blackbody.
[b] Absorbed column density.
[c] Blackbody temperature.
[d] Flux for the entire energy range. Units are ergs/cm^2/s $\times 10^{-X}$, where X is the number inside the parenthesis.

80002013006, 80002013008 and 80002013010). Results of the analysis can be found in Table 3 and are labeled as 'Combined 2013'. The Z^2_3 power can be seen in the right side of Figure 10 and the phase profile in the right hand side of Figure 11. The difference between our best period in this case and Ref. [8] is about 15μs. As expected, the period derivative improved substantially by adding more observations, but it is still one order of magnitude higher than Ref. [8]. The polar magnetic field that we obtained is $B = 2.10(1) \times 10^{14}$G.

One can see in Table 3 that our results and Ref. [8] are not in agreement within statistical errors. However, it is important to note that the calibrated NuSTAR event timestamps for a typical observation are only accurate to $\sim 65\mu$s [30]. This means that there is some scatter of the timestamps around the true arrival time, which can be well approximated by a Gaussian fit with $\sigma \sim 65\mu$s. This uncertainty needs to be taken into account in addition to the statistical uncertainties included already in Table 3 as an instrument effect and therefore a systematic error. Hence, for the combined result, the real period error is $\sigma_{P(tot)} = \sqrt{\sigma^2_{P(stat)} + \sigma^2_{P(syst)}} = \sqrt{(5.68 \times 10^{-08} s)^2 + (65 \times 10^{-6} s)^2} = 65\mu$s. The same happens for the Ref. [8] data, since they are using mainly NuSTAR data. Taking this into account, our period is consistent with their results, since both differs by 15 μs.

Table 3: SGR J1745-29 Timing Analysis

Data	f (**s**$^{-1}$)	$\dot{f}$ (**s**$^{-2}$)	P (**s**)	$\dot{P}$ (**s s**$^{-1}$)	B (**G**)
April 2013	0.2657077(4)	-2(2) $\times 10^{-11}$	$3.7635\mathbf{3}4(6)$	2(3) $\times 10^{-10}$	9(6) $\times 10^{14}$
Combined 2013	0.265707805(4)	-8.08(8) $\times 10^{-13}$	$3.7635\mathbf{3}266(6)$	1.15(1) $\times 10^{-11}$	2.10(1) $\times 10^{14}$
Ref. [8]	0.2657067288(20)	$-4.32(9) \times 10^{-13}$	$3.7635\mathbf{4}7895(29)$	$6.12(12) \times 10^{-12}$	1.53×10^{14}

Finally, we analyzed an additional available, unpublished observation from August 2014 (ID 30002002002) for pulsations using HENDRICS. While no significant pulsation was detected, one of

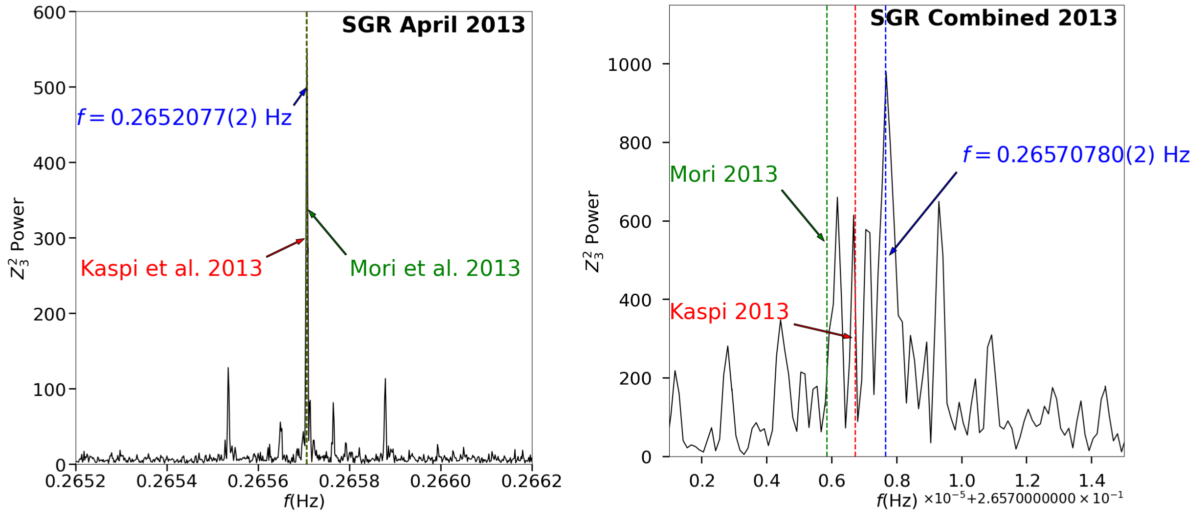

Figure 10: Z_3^2 power of SGR J1745-2900 for the April lightcurves (left) and for the combined observations (right) corresponding to the first ephemeris in [8]. The blue label points to the best frequency obtained in our analysis, the red label (Kaspi et al. 2013) points to the best frequency obtained by [8] for the first ephemeris, and the green label (Mori et al. 2013) corresponds to the best frequency obtained by [7]

the top five candidates with similarly low Z_3^2 power as the other ones, specifically $f = 0.26005886$ s^{-1}, was the closest to the best period identified in the 2013 data. However, its Z_3^2 value was 32, comparable to the other top candidates. In contrast, the Z_3^2 values for the 2013 observations were on the order of thousands (Figure 10).

6 Magnetars as Axion Dark Matter

Before concluding, we would like to propose a thought experiment: the possibility of using magnetars to detect axions, which are favored dark matter candidates. In the past decade, there has been a significant increase in research focused on axions. These particles are particularly intriguing due to their potential as candidates for dark matter and their origin in solving the strong CP problem. Axions also interact with photons, fermions, and baryons, which makes them important in astrophysical contexts where extreme conditions are present.

A novel idea would be a search in which axions from Red Super Giant (RSG) stars could be transformed into photons by the magnetic field of a nearby magnetar in a binary system. This process could result in photons with X-ray energies, potentially detectable by telescopes like NuSTAR. This approach leverages our understanding of axion production in RSG stars, which ranges from 10^45 to 10^47 axions per second. However, initial estimates suggest that the actual axion flux detected by telescopes may be lower than expected, highlighting the need for further detailed investigation in the future. Some additional information is provided in Appendix B.

7 Conclusions

Neutron stars (NSs) are the dense remnants of massive stars, featuring strong magnetic fields and rapid rotation. Magnetars, a rare type of NS, are known for their extremely strong magnetic

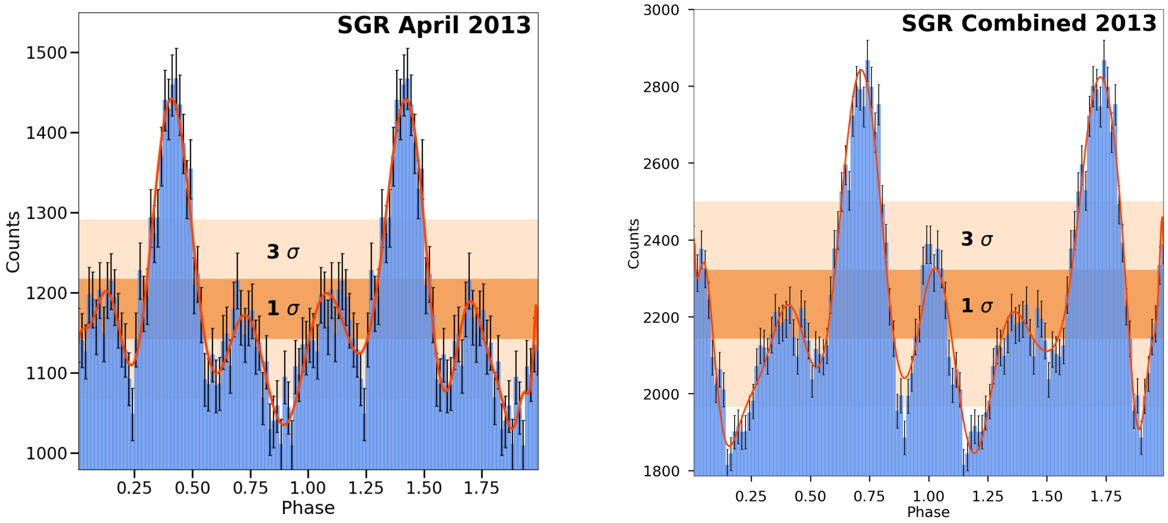

Figure 11: Phase profiles of SGR J1745-2900 were created using the optimal period derived from the April data (left) and the combined NuSTAR observations for the initial ephemeris (right), as detailed in[8]. The 1σ and 3σ confidence bands over the baseline noise are also displayed, with any signal above the 3σ band being of significant physical interest. Finally, a polynomial fit has been applied to guide the eye.

fields and unique behaviors, such as bursts of X-rays and gamma rays. These were discovered thanks to advancements in space-based X-ray telescopes. Instruments like Chandra and NuSTAR have been pivotal in studying magnetars, which exhibit both thermal and non-thermal emissions. One notable magnetar, SGR J1745-29, discovered in 2013 near the Milky Way's supermassive black hole, Sgr A*, has been extensively observed, providing valuable insights into the nature of these extraordinary objects.

In this work, we utilized data from soft and hard X-ray observatories, specifically Chandra, Swift, and NuSTAR, to conduct spectral and timing analysis of SGR J1745-29. Initially, we processed the raw data from these observatories using their respective data processing pipelines to create data files ready for scientific analysis. Subsequently, we employed multi-mission tools to perform advanced studies of the spectral and timing features of the magnetar.

We first verified our processing and science analysis against published 2013 data of the magnetar using NuSTAR and Swift, ensuring the accuracy of our methods for spectral studies. We obtained that the model `TBabs*(Bbody * Bknpower + Gauss)` fits our data best with a $\chi_{red} = 1.02$. The best fit parameters are $N_H = 11.7(1) \times 10^{22}\mathrm{cm}^{-2}$, $kT = 0.90(4)$ keV, $\Gamma_1 = 3.5(1)$, $E_{bk} = 12.5$ keV and $\Gamma_2 = 2.2(1)$. Results are in agreement with typical magnetar values, for which has also been commonly observed that a second power-law component improved the fits in the hard x-ray region. The simple power-law seems to be a worse fit to our data than the same model fit in Ref. [7], for which they obtain a reduced χ^2 close to 1. This may be due to the fact that we are using fewer Swift observations than Ref. [7], resulting in reduced statistics in the low energy range.

We then analyzed 11 years of monitoring data from Chandra to examine the long-term evolution of spectral features, i.e. the blackbody temperature and soft X-ray flux, and tested a tentative claim of an unexpected temperature increase in the 2022 Chandra data set by the TFG [10]. Our results are in agreement with a flat temperature around 0.7 keV from 2016 to

2023 contrary to the hint previously found. Chandra's subarcsec angular resolution, allow us to unequivocally distinguish the magnetar from other sources in the crowded SgrA* region. On the other hand, Chandra is more sensitive in the soft x-ray band for which the blackbody dominantes. Hence, our results rule out a possible increase in the temperature in the year 2022. This results are in agreement with the 3.5 years follow-up made by Ref. [9].

Additionally, we used unpublished hard X-ray NuSTAR data to attempt characterizing the temporal evolution of the magnetar's hard X-ray emission but found the results inconclusive. NuSTAR angular resolution is incapable of resolving the magnetar from the X-ray transients that were appearing during the years 2014-15-16, affecting hugely the results. This is even more relevant since the magnetar flux decreased considerably during the years following the outburst in 2013, according to our Chandra results, making the transients the dominant sources.

For the timing analysis, we initially developed Python code but ultimately relied on HENDRICS, which performed somewhat better than our code. We verified the analysis process against published results and studied new data from NuSTAR taken in 2014; however, no strong pulsations were detected. This may be due to low statistics since the flux is much lower and a transient was appearing during this observation.

Lastly, we proposed using magnetars in binaries with supergiants as dark matter laboratories to search for axions in Appendix B . Preliminary calculations suggest that the expected number of photons from axion conversion would be impractically low.

Future work on SGR J1745-29 and other magnetars will leverage advancements in X-ray observatories and data analysis techniques. Enhanced spectral and timing methods, alongside new observational campaigns, will provide deeper insights into magnetar emissions. Future missions, like HEX-P as the proposed follow-up to NASA's NuSTAR, promise higher resolution and sensitivity, potentially resolving current ambiguities. Additionally, exploring magnetars in binary systems with supergiants as dark matter laboratories remains an intriguing, though challenging, prospect. Continued efforts in both observational and theoretical studies will expand our understanding of these fascinating cosmic objects.

References

[1] SA Olausen and et al. The mcgill magnetar catalog. The Astrophysical Journal Supplement Series, 212(1):6, 2014.

[2] Robert C Duncan and et al. Formation of very strongly magnetized neutron stars: Implications for gamma-ray bursts. Astrophysical Journal, Part 2-Letters, 392:L9–L13, 1992.

[3] Martin C Weisskopf and et al. Chandra x-ray observatory (cxo): overview. X-ray optics, instruments, and missions iii, 4012:2–16, 2000.

[4] David N Burrows and et al. The swift x-ray telescope. Space science reviews, 120:165–195, 2005.

[5] Fiona A Harrison and et al. The nuclear spectroscopic telescope array (nustar) high-energy x-ray mission. The Astrophysical Journal, 770(2):103, 2013.

[6] JA Kennea and et al. Swift discovery of a new soft gamma repeater, sgr j1745-29, near sagittarius a. The Astrophysical Journal Letters, 770(2):L24, 2013.

[7] Kaya Mori and et al. Nustar discovery of a 3.76 s transient magnetar near sagittarius a. The Astrophysical Journal Letters, 770(2):L23, 2013.

[8] Victoria M Kaspi and et al. Timing and flux evolution of the galactic center magnetar sgr j1745-2900. The Astrophysical Journal, 786(2):84, 2014.

[9] Coti Zelati and et al. Chandra monitoring of the galactic centre magnetar sgr j1745-2900 during the initial 3.5 years of outburst decay. Monthly Notices of the Royal Astronomical Society, 471(2):1819–1829, 2017.

[10] Martina Cans Cugat. Análisis de datos observacionales de rayos x. Bachelor's thesis, University of Zaragoza, 2023.

[11] James M Lattimer and et al. The physics of neutron stars. Science, 304(5670):536–542, 2004.

[12] Chryssa Kouveliotou and et al. An x-ray pulsar with a superstrong magnetic field in the soft γ-ray repeater sgr1806-20. Nature, 393(6682):235–237, 1998.

[13] PC Gregory and et al. An extraordinary new celestial x-ray source. Nature, 287(5785):805–806, 1980.

[14] Christopher Thompson and et al. The soft gamma repeaters as very strongly magnetized neutron stars. ii. quiescent neutrino, x-ray, and alfven wave emission. The Astrophysical Journal, 473(1):322, 1996.

[15] Lilia Ferrario and et al. Origin and evolution of magnetars. Monthly Notices of the Royal Astronomical Society: Letters, 389(1):L66–L70, 2008.

[16] Michael P Muno and et al. A neutron star with a massive progenitor in westerlund 1. The Astrophysical Journal, 636(1):L41, 2005.

[17] J Simon Clark and et al. A vlt/flames survey for massive binaries in westerlund 1-iv. wd1-5–binary product and a pre-supernova companion for the magnetar cxou j1647-45? Astronomy & Astrophysics, 565:A90, 2014.

[18] Jonathan Braithwaite and et al. Axisymmetric magnetic fields in stars: relative strengths of poloidal and toroidal components. Monthly Notices of the Royal Astronomical Society, 397(2):763–774, 2009.

[19] Kōji Uryū and et al. Equilibrium solutions of relativistic rotating stars with mixed poloidal and toroidal magnetic fields. Physical Review D, 90(10):101501, 2014.

[20] Christopher Thompson and Robert C Duncan. The giant flare of 1998 august 27 from sgr 1900+ 14. ii. radiative mechanism and physical constraints on the source. The Astrophysical Journal, 561(2):980, 2001.

[21] C Thompson and et al. Electrodynamics of magnetars: implications for the persistent x-ray emission and spin-down of soft gamma repeaters and anomalous x-ray pulsars. The Astrophysical Journal, 574(1):332, 2002.

[22] Roberto Turolla and et al. Magnetars: the physics behind observations. a review. Reports on Progress in Physics, 78(11):116901, 2015.

[23] Sandro Mereghetti and et al. The strongest cosmic magnets: soft gamma-ray repeaters and anomalous x-ray pulsars. The Astronomy and Astrophysics Review, 15(4):225–287, 2008.

[24] Maxim Lyutikov, Fotis P Gavriil, and et al. Resonant cyclotron scattering and comptonization in neutron star magnetospheres. Monthly Notices of the Royal Astronomical Society, 368(2):690–706, 2006.

[25] Paolo Esposito and et al. Magnetars: a short review and some sparse considerations. Timing Neutron Stars: Pulsations, Oscillations and Explosions, pages 97–142, 2021.

[26] Riccardo Giacconi and et al. An x-ray scan of the galactic plane from uhuru. Astrophysical Journal, 165:L27, 1971.

[27] Finn E Christensen and et al. X-ray optics for astrophysics: a historical review. In Handbook of X-ray and Gamma-ray Astrophysics, pages 73–114. Springer, 2024.

[28] Riccardo Giacconi, Bruno Rossi, and et al. A "telescope" for soft x-ray astronomy. Journal of Geophysical Research, 65(2):773–775, 1960.

[29] Hans Wolter. Spiegelsysteme streifenden einfalls als abbildende optiken für röntgenstrahlen. Annalen der Physik, 445(1-2):94–114, 1952.

[30] Matteo Bachetti and et al. Timing calibration of the nustar x-ray telescope. The Astrophysical Journal, 908(2):184, 2021.

[31] W A Joye and et al. New features of saoimage ds9. In Astronomical data analysis software and systems XII, volume 295, page 489, 2003.

[32] Keith Arnaud and et al. Xspec: An x-ray spectral fitting package. Astrophysics Source Code Library, pages ascl–9910, 1999.

[33] Matteo Bachetti and et al. Hendrics: High energy data reduction interface from the command shell. Astrophysics Source Code Library, pages ascl–1805, 2018.

[34] Julia K. Vogel and et al. Nustar observations of the magnetar 1e 2259+586. The Astrophysical Journal, 789(1):75, 2014.

[35] Nanda Rea, Paolo Esposito, José A Pons, Roberto Turolla, Diego F Torres, Gian Luca Israel, Andrea Possenti, Marta Burgay, Daniele Viganò, Alessandro Papitto, et al. A strongly magnetized pulsar within the grasp of the milky way's supermassive black hole. The Astrophysical Journal Letters, 775(2):L34, 2013.

[36] OC De Jager and et al. A powerful test for weak periodic signals with unknown light curve shape in sparse data. Astronomy and Astrophysics, 221:180–190, 1989.

[37] Douglas Clowe and et al. A direct empirical proof of the existence of dark matter. The Astrophysical Journal, 648(2):L109, 2006.

[38] Roberto D Peccei and et al. Cp conservation in the presence of pseudoparticles. Physical Review Letters, 38(25):1440, 1977.

[39] RJ Crewther and et al. Chiral estimate of the electric dipole moment of the neutron in quantum chromodynamics. Physics Letters B, 88(1-2):123–127, 1979.

[40] Christopher Abel and et al. Measurement of the permanent electric dipole moment of the neutron. Physical Review Letters, 124(8):081803, 2020.

[41] Doron Chelouche and et al. Spectral signatures of photon–particle oscillations from celestial objects. The Astrophysical Journal Supplement Series, 180(1):1, 2008.

[42] Francesca Chadha-Day and et al. Axion dark matter: What is it and why now? Science advances, 8(8):eabj3618, 2022.

[43] Peter W Graham and et al. Experimental searches for the axion and axion-like particles. Annual Review of Nuclear and Particle Science, 65:485–514, 2015.

[44] Samuel J Witte and et al. Axion-photon conversion in neutron star magnetospheres: The role of the plasma in the goldreich-julian model. Physical Review D, 104(10):103030, 2021.

[45] AI Bogomazov and et al. Magnetars, gamma-ray bursts, and very close binaries. Astronomy reports, 53:325–333, 2009.

[46] Andrei M Beloborodov and et al. Corona of magnetars. The Astrophysical Journal, 657(2):967, 2007.

[47] Mengjiao Xiao and et al. Constraints on axionlike particles from a hard x-ray observation of betelgeuse. Physical Review Letters, 126(3):031101, 2021.

[48] Georg Raffelt and et al. Mixing of the photon with low-mass particles. Physical Review D, 37(5):1237, 1988.

[49] Jean-François Fortin and et al. Constraining axion-like-particles with hard x-ray emission from magnetars. Journal of High Energy Physics, 2018(6):1–22, 2018.

[50] Jean-François Fortin and et al. Magnetars and axion-like particles: probes with the hard x-ray spectrum. Journal of Cosmology and Astroparticle Physics, 2021(06):036, 2021.

[51] James J Condon and et al. Essential radio astronomy, volume 2. Princeton University Press, 2016.

Appendix

A Minimum Magnetic Field Strength in a Neutron Star

A.1 Radiation from an Accelerated Charge

A static charge q produces a purely radial electric field $\vec{E} = |E_r|\vec{u_r}$. Let's suppose a charge initially at rest that is accelerated to a small velocity $\Delta v \ll c$ in a time Δt. This produces a distortion of the radial field lines, that travels at the speed of light. Radially, the perturbation will have propagated to $r = ct$ and, defining a θ angle between the acceleration vector and the line of sight connecting the charge to the observer, and the perpendicular component of the electric field is:

$$\frac{E_\perp}{E_r} = \frac{\Delta v t \sin\theta}{c\Delta t}. \tag{14}$$

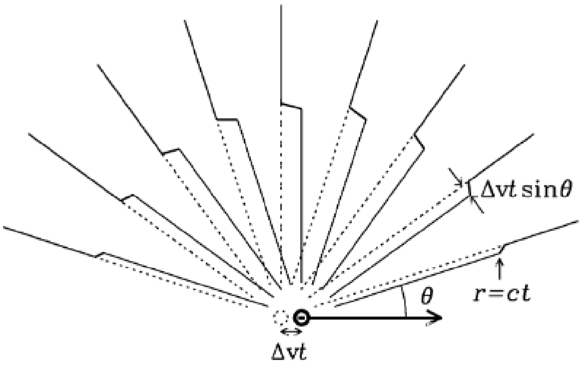

Figure A1: The diagram illustrates the electric field lines produced by an accelerating electron. The dotted circle marks the electron's initial location, with dotted lines representing the radial lines of force extending from that point. At time t after a small acceleration $\Delta v/\Delta t$, the electron has shifted by Δvt, and its lines of force have transversely displaced by $\Delta vt \sin\theta$ (From [51])

Now, one can use the Coulomb's law for the magnitude of the electric field:

$$E_r = \frac{q}{r^2}, \tag{15}$$

now substituting in Equation 14 and using $t = r/c$ we have:

$$E_\perp = \frac{q}{r^2}\left(\frac{\Delta v}{\Delta t}\right)\frac{r\sin\theta}{c^2}, \tag{16}$$

and if one considers that:

$$\dot{v} \equiv \lim_{\Delta t\to 0}\left(\frac{\Delta v}{\Delta t}\right), \tag{17}$$

this yields:

$$E_\perp = \frac{q\dot{v}\sin\theta}{rc^2}. \tag{18}$$

Since the perpendicular component of the electric field to the line of sight decays slower with distance ($E_\perp \propto r^{-1}$) than the radial component ($E_r \propto r^{-2}$), for an observer placed far from the source, the perpendicular component is the dominant one, resulting in the fact that the electric field is linearly polarized in the perpendicular direction to the line of sight (los).

Now, in order to obtain how much power is emitted in each direction, one must compute the Poynting flux:

$$\vec{S} = \frac{c}{4\pi}\vec{E} \times \vec{B}, \tag{19}$$

in CGS units we have that $|\vec{E}| = |\vec{B}|$ so:

$$|\vec{S}| = \frac{c}{4\pi}E^2, \tag{20}$$

and inserting Equation 18 we have:

$$|\vec{S}| = \frac{c}{4\pi}\left(\frac{q\dot{v}\sin\theta}{rc^2}\right)^2 = \left(\frac{q^2\dot{v}^2}{4\pi c^3}\right)\frac{\sin^2\theta}{r^2}, \tag{21}$$

where if we consider large distances, we can assume that that $|E| = |E_\perp$.

The charged particle emits radiation following a dipolar power distribution, proportional to $\sin^2(\theta)$, resembling a doughnut shape with its axis aligned parallel to the acceleration vector v.

The total power emitted is the integral of $|\vec{S}|$ over the surface of a sphere of raius r:

$$\begin{aligned} P &= \int_{\text{sphere}} |\vec{S}|dA = \frac{q^2\dot{v}^2}{4\pi c^3}\int_{\phi=0}^{2\pi}\int_{\theta=0}^{\pi}\frac{\sin^2\theta}{r^2}r\sin\theta d\theta r d\phi \\ &= \frac{q^2\dot{v}^2}{2c^3}\int_{\theta=0}^{\pi}\sin^3\theta d\theta, \end{aligned} \tag{22}$$

and with the integral being 4/3 one has that the total power emitted is:

$$P = \frac{2}{3}\frac{q^2\dot{v}^2}{c^3}, \tag{23}$$

the Larmor's equation.

A.2 Magnetic Dipole Radiation

The inclination of the magnetic dipole from the rotation axis, emits electromagnetic radiation at the rotation frequency. In order to derive this radiation, one has to take into account first the Larmor's equation (Equation 23) and use that the electric dipole moment is $p = qr$ and its component perpendicular to the rotation axis is $p_\perp = p\sin\alpha$, then we have that:

$$P_{\text{rad}} = \frac{2q^2\dot{v}^2}{3c^3} = \frac{2}{3}\frac{(q\ddot{r}\sin\alpha)^2}{c^3} = \frac{2}{3}\frac{(\ddot{p}_\perp)^2}{c^3}. \tag{24}$$

Taking into account that the Gaussian CGS units for the magnetic and the electric field are the same, then the power of magnetic dipole radiation is:

$$P_{\text{rad}} = \frac{2}{3}\frac{(\ddot{m}_\perp)^2}{c^3}, \tag{25}$$

where $m_\perp = m\sin\alpha$. The magnetic dipole moment's magnitude for a sphere with uniform magnetization, having a radius R and a surface magnetic field strength B, is

$$m = BR^3. \tag{26}$$

Finally, considering that the inclined magnetic dipoles rotates with angular velocity $\Omega = 2\pi/P$ being P the pulsar period, then we have that the magnetic dipole radiation is:

$$P_{\text{rad}} = \frac{2}{3}\frac{m_{\perp}^2 \Omega^4}{c^3} = \frac{2}{3c^3}\left(BR^3 \sin\alpha\right)^2 \left(\frac{2\pi}{P}\right)^4. \tag{27}$$

A.3 Spin-Down Luminosity

The kinetic energy of rotation, E, for an object in spin is determined by its moment of inertia, I, through

$$E = \frac{I\Omega^2}{2} = \frac{2\pi^2 I}{P^2}. \tag{28}$$

The moment of inertia of a sphere of radius R, mass M and uniform density spinning about its z-axis is

$$I = \frac{2MR^2}{5}. \tag{29}$$

As we mentioned before, magnetic dipole radiation extracts rotational energy, it slowly increases the pulsar period

$$\dot{P} \equiv \frac{dP}{dt} > 0, \tag{30}$$

where the period derivative is dimensionless. Now, one can make the derivative of the kinetic energy of rotation:

$$-\dot{E} \equiv -\frac{dE_{\text{rot}}}{dt} = -\frac{d}{dt}\left(\frac{1}{2}I\Omega^2\right) = -I\Omega\dot{\Omega}, \tag{31}$$

this is usually called the spin-down luminosity, which refers to the measured loss rate of rotational energy, presumed to be equivalent to the luminosity produced by magnetic dipole radiation. It is possible to express it in terms of the period and its derivative, using $\Omega = 2\pi/P$ and $\dot{\Omega} = 2\pi\left(-P^{-2}\dot{P}\right)$ one arrives at:

$$-\dot{E} = \frac{4\pi^2 I\dot{P}}{P^3} \tag{32}$$

A.4 Minimum Magnetic Field Strength

It is usually assumed that the measured loss rate of rotational energy is equivalent to the luminosity produced by magnetic dipole radiation, so we have that $-\dot{E} \approx P_{\text{rad}}$. Then, using the results that we obtained in the previous subsections of the appendix, specifically Equations 32 and 27, can be used to yield a lower limit to the magnetic field strength ($B < B\sin\alpha$) at the neutron surface, where α is the angle between the dipolar magnetic field direction and the rotation axis of the NS. Using all the above equations:

$$\begin{gathered}
P_{\text{rad}} = -\dot{E}, \\
\frac{2}{3c^3}\left(BR^3\sin\alpha\right)^2\left(\frac{4\pi^2}{P^2}\right)^2 = \frac{4\pi^2 I\dot{P}}{P^3}, \\
B^2 = \frac{3c^3 IP\dot{P}}{2\cdot 4\pi^2 R^6 \sin^2\alpha}, \\
B > \left(\frac{3c^3 I}{8\pi^2 R^6}\right)^{1/2} (P\dot{P})^{1/2}.
\end{gathered} \tag{33}$$

If we take into account common values for the pulsar parameters, we have that:

$$\left[\frac{3\cdot\left(3\times10^{10}\ \mathrm{cm\ s^{-1}}\right)^{3}\cdot10^{45}\ \mathrm{g\ cm^{2}}}{8\pi^{2}\left(10^{6}\ \mathrm{cm}\right)^{6}}\right]^{1/2}\approx3.2\times10^{19}, \tag{34}$$

then, we finally get the desired result:

$$B>3.2\times10^{19}\sqrt{P\dot{P}/\mathrm{s}}\quad\mathrm{G}, \tag{35}$$

usually called the characteristic magnetic field of a pulsar.

A.5 Characteristic Age

If we take into account that the spin-down luminosity is equal to the magnetic dipole radiation luminosity and $B\sin\alpha$ doesn't change significantly with time, one can estimate the pulsar's age from $P\dot{P}$ on the assumption that the pulsar's initial period P_0 was much shorter than its current period. Solving Equation 33, for $P\dot{P}$ one can show that in that case $P\dot{P}$ also doesn't change significantly with time. Rewriting $P\dot{P}=P\dot{P}$ as $PdP=P\dot{P}dt$ and intregating over the pulsar's age τ gives:

$$\int_{P_0}^{P}PdP=\int_{0}^{\tau}(P\dot{P})dt=P\dot{P}\int_{0}^{\tau}dt \tag{36}$$

since $P\dot{P}$ is considerated constant. The integrated result of the last equation is:

$$\frac{P^2-P_0^2}{2}=P\dot{P}\tau \tag{37}$$

which in the limit where the initial period is much lower than the actual one, the characteristic age of the pulsar:

$$\tau\equiv\frac{P}{2\dot{P}} \tag{38}$$

should be close to the actual pulsar age.

B Axion and the Strong CP Problem

B.1 Axions and Axion-Like Particles

The QCD Lagrangian of the Standard Model (SM), describes the strong interaction within the SM based on the local gauge invariance of the $SU(3)_c$ group. The most comprehensive gauge-invariant Lagrangian of QCD can be expressed as follows:

$$\mathcal{L}_{\mathrm{QCD}}=-\frac{1}{4}G^{a}_{\mu\nu}G^{\mu\nu}_{a}+\sum_{f}\bar{\psi}_f\left(i\gamma^{\mu}D_{\mu}-m_f\right)\psi_f+\frac{\theta g^2}{32\pi^2}G^{a}_{\mu\nu}\tilde{G}^{\mu\nu}_{a} \tag{39}$$

where the first term in the Lagrangian describes the dynamics of the gluon fields, including their self-interactions, which are a distinctive feature of QCD not found in other gauge theories like QED. The second term describes the quarks, their interactions with the gluon fields, and their masses. Finally, the last term , the so called θ-term, emerges as a direct outcome of the spontaneous breaking of the axial $U(1)_A$ symmetry in the QCD Lagrangian. However, the existence of this term in the Lagrangian leads to another fundamental problem called the strong CP violation. It disrupts the PT (parity-time) symmetry, while conserving the C (charge conjugation) symmetry, which makes it a source of CP violation within the strong interaction.

However, there is no experimental indication of CP violation in the strong interactions. The most relevant prove is the measure of the electric dipole moment of the neutron, which actual bound value is $d_{\mathrm{n}} = (0.0 \pm 1.1_{\mathrm{stat}} \pm 0.2_{\mathrm{sys}}) \times 10^{-26} e \cdot \mathrm{cm}$,[40], and can be related to the θ value within the chiral perturbation theory [39], resulting in a θ-value of the order $|\theta| \lesssim 10^{-10}$.

The smallness of this θ value was was not understood until Peccei et al [38] proposed the axion model. They postulated the existence of an additional global chiral $U(1)$ symmetry within the standard model Lagrangian, called the Peccei-Quinn symmetry in honor of their contributions. This symmetry undergoes spontaneous breaking at a high energy scale f_a, leading to the emergence of a massless Nambu-Goldstone Boson (NGB) known as the *axion*. Introducing this symmetry into the theory effectively transforms the θ vacuum angle into a dynamic CP-conserving field referred to as the axion field,

$$\frac{g_s^2}{32\pi^2} \theta G^a_{\mu\nu} \tilde{G}^{a\mu\nu} \to \frac{1}{2} (\partial_\mu a)^2 + \frac{g_s^2}{32\pi^2} \left(\theta + \frac{a}{f_a} \right) G^a_{\mu\nu} \tilde{G}^{a\mu\nu}, \tag{40}$$

where f_a is a model dependent energy scale. When the effective potential of the axion reaches its minimum, the dependence on θ cancels out, resolving the strong CP problem altogether. The consideration of the nontrivial vacuum structure and the consideration of instanton effects makes the circle of minimum potential to become tilted, breaking explicitly the PQ symmetry, which leads the axion to acquire mass ($m_a \neq 0$).

The gluonic term in Equation 40 express the axion-gluon interaction, allowing the mixing with mesons. The interaction between the axion and the neutral pion results in the generation of a slight mass for the axion, derived from the mass of the pion. This phenomenon occurs only because the axion and the pion share identical quantum numbers. This means that there is a proportionality relation between both masses:

$$m_a f_a \sim m_\pi f_\pi, \tag{41}$$

where f_a is proportional to the energy at which the PQ symmetry is spontaneously broken, m_π is the pion mass, and f_π is a constant determined from the pion decay rate through the weak interaction. The axion mass is ([42])

$$m_a = \frac{m_\pi f_\pi}{f_a} \frac{\sqrt{m_u m_d}}{m_u + m_d} \simeq 6 \times 10^{-6} \mathrm{eV} \left(\frac{10^{12} \mathrm{GeV}}{f_a} \right). \tag{42}$$

B.2 Axion Searches Using Magnetars

The past decade has seen a surge in activity surrounding axion research (see e.g. [43] for a review). The potential of axions as dark matter candidates, combined with their origin from a well-founded solution to the strong CP problem, renders the field of axion research particularly interesting. Moreover, the relevance of axions extends further due to their interactions with photons, fermions, and baryons, making them significant in astrophysical settings, where we encounter the most extreme conditions imaginable. In particular, axions can be produced in stars, like our Sun, through their coupling to photons. This coupling is based on the Primakoff effect, i.e. the axion can transform into a photon (and vice versa) in the presence of an external, uniform magnetic field that is transverse to the particle's propagation. The expression of the conversion probability in vacuum is the following:

$$P_{a\to\gamma} = \left(\frac{BLg_{a\gamma}}{2}\right)^2 \left(\frac{\sin(qL/2)}{qL/2}\right)^2, \tag{43}$$

where B is the magnetic field, L the magnet length, $g_{a\gamma}$ the axion-photon coupling and q is the momentum of the axion:

$$q = \frac{m_a^2}{2E_a}. \tag{44}$$

It is noticeable from Equation 43 that the conversion probability is proportional to the magnetic field B^2 and the length over which B is uniform. On the other hand, we have learned that the magnetic fields of magnetars are the most extreme in the universe ($B_p \sim 10^{15}$ G), so a natural question arise: Could magnetars be the astrophysical experiment that we need to finally discover the axion?

Usually, there are two approaches to this problem: the dark matter (halo) axions interact with the immense magnetic field of the magnetar, producing a signal in radio waves, or the axions emitted inside the magnetar are the ones that interact, producing a high energy signal in the X-ray regime (the one interesting for us since we are working with X-ray telescopes). The second approach, requires a model for the axion production inside the magnetar. However, our knowledge about the internal physics of neutron stars, as well as the magnetosphere, is limited, so an estimation of the axion magnetar flux is not straightforward. In the literature one can find many attempts to develop a successful model [44, 41].

Obviously, the conversion probability in the magnetosphere is not as simple as Equation 43, since one may take into account the approximate dipole nature of the magnetic field far from the surface, as well as plasma effects due to the electric currents that are formed in the magnetosphere. The first successful attempt to calculate the probability $P_{a\gamma}$ in the dipolar magnetic field near neutron stars, while considering the non-zero refractive indices of photons in the strong magnetic field, was performed by Georg Raffelt et al. in 1988 [48]. They computed $P_{a\gamma}$ near the neutron star surface, and concluded that it was too small to be observed, using typical values of the magnetic field and $g_{a\gamma} \sim 10^{-10}\text{GeV}^{-1}$. However, the numerical solution of the full propagation equations was presented in [49], where they obtained that the conversion probability actually becomes substantial near a radius of conversion $r_{a\gamma}$. The ALP-photon mixing matrix includes an off-diagonal term that is proportional to the magnetic field, with a parametric dependence on the radial distance r of the order $\propto g_{a\gamma}B_0/r^3$, where B_0 is the magnetic field at the surface. The diagonal terms include the axion mass m_a and the photon mass m_γ, both derived from the refractive indices, with a dependence on $r \sim 1/r^6$. At the surface ($r = r_0$), the photon mass term is dominant, resulting in a small mixing angle. Far from the surface ($r \gg r_0$), the axion mass term becomes dominant, and the mixing angle is small again. However, in the intermediate region, around the "radius of conversion" $r_{a\gamma} \sim 1000r_0$ (r_0 corresponds to the magnetar radius), the off-diagonal mixing term becomes comparable to the diagonal photon mass term, leading to a significant mixing angle. It is in this region that ALP-photon conversion occurs [50].

In this instance, an entirely novel strategy is suggested: the transformation of axions from Red Super Giants RSG into photons, facilitated by the magnetic field of a neighboring magnetar with which it forms a binary system. This is relevant to our work, as the photons converted in this process would possess X-ray energies, potentially making them detectable by a telescope such as NuSTAR. The main advantage of this approach is that the production of high energy axions inside a RSG is better known, our knowledge about stars is wider (c.f. Ref. [47], for a study constraining the axion-photon coupling with Betelgeuse). Typical values for the total number of axions per second produced in RSG stars ranges from 10^{45}axs/s to 10^{47}axs/s. However, a rough estimate was done in Appendix B.3, showing that the actual axion flux converted in the magnetosphere and detected by our telescopes may be lower than expected. In any case, a more detailed study may be carried out in the future.

B.3 A Rough Estimate

Using the results from Figure 15 in Ref. [50], the maximum conversion probability for an axion with energy $w = 20$ keV, axion coupling $g_{a\gamma} = 10^{-10}\text{GeV}^{-1}$, $m_a = 10^{-6}$ eV, $r_0 = 10$ km, and $\theta = \pi/2$ (θ is the polar angle taking the rotational axis as a reference) is $P_{a\gamma} \sim 0.003$. The expected number of photons at the detector depends on the transmission probability in the magnetar $P_{a\gamma}$, where axions are converted into X-rays, the efficiency of the detector ϵ, the exposure time Δt, and the number of axions emitted N_{aE} that finally arrive at the detector. The final expression is the following:

$$N_\gamma = N_{aE}\frac{A}{4\pi d^2}\epsilon \Delta t P_{a\gamma}, \tag{45}$$

where d is approximately the distance between the binary system and the Earth (neglecting the distance between the magnetar and the RSG). For specific values:

$$N_\gamma/s = 10^{45}\frac{\text{axs}}{s}\frac{1\text{m}^2}{4\pi \times (2.5\text{kpc})^2\frac{(3.086\times 10^{19}\text{m})^2}{1\text{kpc}^2}} \times 1 \times 0.003 \approx 40.11\text{cts/s}\ . \tag{46}$$

Here, we assume that the detector efficiency for 20 keV is $\epsilon = 1$. For the number of axions emitted, a typical value of 10^{45}axs/s is assumed, and the distance $d = 2.5$ kpc corresponds to the distance between the Earth and LS 5039, an X-ray binary that is a candidate to contain a magnetar. This is a rough estimate since we are considering that all the axions emitted in the cone formed by the center of the RSG and the area of our detector are affected by the same conversion probability. However, conversion only occurs in a region that is $\sim 1000 r_0$. Assuming a magnetar approaching the line of sight, conversion will only occur in a specific small area. Let's assume that the conversion probability of 0.003 is maintained across a 10-meter region (consistent with Figure 15, right top panel from [50]). Assuming a distance of 100 AU between the star and the magnetar, one can calculate the fraction of axions that cross the 10 m circular region and the telescope aperture. The solid angle (in steradians) subtended by the circle at the star's location is given by:

$$\Omega_{\text{circle}} = \frac{\pi \times R^2}{d^2_{\text{S-circle}}} \approx 1.40 \times 10^{-25} \text{ steradians} \tag{47}$$

where $R = 10$ m is the radius of the circle and $d_{\text{S-circle}} = 100$ AU $= 1.496 \times 10^{13}$ meters is the typical distance between the magnetar and the RSG. The number of axions crossing that region

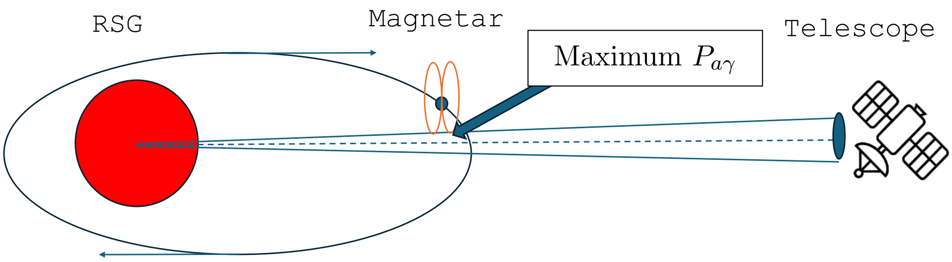

Figure A2: Schematic view of the calculation. The RSG is on the left, the magnetar in the middle and the telescope on the right. Even thought the number of axions arriving to the detector is determined by the cone that is formed between the center of the star and the aperture area, the conversion is only substantial in the radius of conversion $r_{a\gamma} \sim 1000 r_0$

is:

$$N_{aA} = N_{aE} \frac{\Omega}{4\pi} = 10^{45} \frac{\text{axs}}{s} \times \frac{1.40 \times 10^{-25}}{4\pi} \approx 7.5 \times 10^{19} \frac{\text{axs}}{s} \tag{48}$$

Then, considering these axions as emitted from a point source (since the magnetar is far from the Earth), we have:

$$N_\gamma / s = 7.5 \times 10^{19} \frac{\text{axs}}{s} \frac{1\text{m}^2}{4\pi \times (2.5\text{kpc})^2 \frac{(3.086 \times 10^{19}\text{m})^2}{1\text{kpc}^2}} \times 1 \times 0.003 \approx 7.5 \times 10^{-23} \text{cts/s} \tag{49}$$

where we have approximated the distance from the magnetar to the Earth as the distance from the binary to the Earth.

C Information About the Observations Used in This Work

Table C1 contains information about all the Swift, Chandra and NuSTAR observation that were analyzed in this work. The ID column contains the mission-specific and unique observation identification numbers of each observation. The start of each observation is provided in date and Modified Julian Date (MJD). The last column reflects the exposure (exp) time for each observation in ksec.

D The H-Test to Find the Best Period

Periodic signals are crucial in Astronomy, it shows us that the objects that we are observing are full of live, interacting with their environment and undergoing many complex effects. In our case, the first step to identify a magnetar is to perform a time analysis of the light curve, this basically consists in folding the arrival times on the phase interval $(0, 1)$ or $(0, 2\pi)$ using the proper period and its derivative. This is practically done by subtracting to each of the light curves times a

Table C1: Observations used in the Chandra, NuSTAR, and Swift studies of SGR J1745-29

Observatory	**ID**	**MJD**	**Date**	**Exp (ks)**
NuSTAR	80002013002	56410	2013-04-27 06:16:07	49.69
NuSTAR	30001002006	56408	2013-04-26 01:01:07	37.06
NuSTAR	80002013004	56408	2013-05-04 17:31:07	38.52
NuSTAR	80002013006	56423	2013-05-11 14:26:07	32.70
NuSTAR	80002013008	56430	2013-05-18 17:36:07	38.83
NuSTAR	80002013010	56439	2013-05-27 10:16:07	37.31
NuSTAR	30002002002	5690	2014-08-30 19:46:07	60.30
NuSTAR	30002002008	57112	2015-03-31 04:41:07	25.71
Swift	00554491001	56409	2013-04-25 20:50:29	19.65
Swift	00035650242	56409	2013-04-26 16:01:59	4.70
Chandra	13839	56132	2012-07-24 07:02:59	176.25
Chandra	15043	56549	2013-09-14 00:03:46	50.07
Chandra	16214	56833	2014-05-20 00:18:05	50.07
Chandra	16218	56986	2014-10-20 08:21:21	40.07
Chandra	16966	57192	2015-05-14 08:45:44	25.07
Chandra	18732	57590	2016-07-18 12:00:30	84.47
Chandra	19703	57953	2017-07-15 22:34:58	89.30
Chandra	20346	58236	2018-04-24 03:32:34	33.07
Chandra	20347	58237	2018-04-25 03:36:14	36.07
Chandra	20446	58689	2019-07-21 00:00:14	57.67
Chandra	21453	58576	2019-03-29 04:02:30	33.07
Chandra	21455	58578	2019-03-31 05:19:02	33.07
Chandra	21456	58579	2019-04-01 04:21:56	33.07
Chandra	22230	58685	2019-07-17 22:51:26	57.67
Chandra	22604	58938	2020-03-26 04:41:38	33.07
Chandra	22592	59361	2021-05-23 01:46:20	21.52
Chandra	23665	59318	2021-04-10 06:33:08	25.07
Chandra	23666	59319	2021-04-11 06:19:45	25.07
Chandra	23668	59324	2021-04-16 08:25:05	25.07
Chandra	24361	59830	2022-09-23 04:34:00	30.08
Chandra	25297	59643	2022-03-20 05:03:51	25.91
Chandra	25298	59645	2022-03-22 06:19:15	25.09
Chandra	26757	60032	2023-04-13 06:06:45	24.59
Chandra	26758	60035	2023-04-16 05:40:17	25.09

reference time, then ones divide by the period and subtract the remainder:

$$\theta_i = (t - t_0)\, f + \frac{1}{2}\dot{f}\,(t - t_0)^2 \tag{50}$$

where θ_i $(i = 1, 2, ..., n)$ are the phases corresponding to each of the time step. This interval represents one full period, which in the absence of periodicity consists of an uniform distribution of the folded events, if the source frequency is larger than the mean count rate, and one can perform a test of uniformity on the circle.

The most used test of uniformity on the circle is the *H-test*, which is based on the Z_m^2-test where the number of harmonics m is optimized.The Z_m^2 test involves the sum of the Fourier powers of the first m harmonics:

$$Z_m^2 = 2n\sum_{k=1}^{m}(\frac{1}{n}\sum_{i=1}^{n}\cos k\theta_i + \frac{1}{n}\sum_{i=1}^{n}\sin k\theta_i) = 2n\sum_{k=1}^{m}(\hat{\alpha}_k^2 + \hat{\beta}_k^2) \tag{51}$$

where we have defined the empirical trigonometric moments $\hat{\alpha}_k$ and $\hat{\beta}_k$

The H-test consists of the following, m is specified as some suitable function of the data θ_i using Hart's rule. His rule amounts to calculating the value of m, called by M, that minimizes an estimator of the mean integrated squared-error MISE between the Fourier Series Estimator and the true unknown light curve. Then the M is the one the maximizes

$$\max_{1 \lesssim m < \infty} \left(Z_m^2 - 4m + 4\right) = Z_M^2 - 4M + 4. \tag{52}$$

However, computationally is impossible to scan over an infinite number of harmonics and usually is truncated at 20, leading us to the definition of the H-statistic [36] :

$$H \equiv \max_{1 \lesssim m < 20} \left(Z_m^2 - 4m + 4\right) = Z_M^2 - 4M + 4. \tag{53}$$

D.1 The Z_3^2-Test

In practice, including only the first three harmonics in Equation (51) (m=3) strikes a balance between capturing the complexity of real periodic signals and managing computational efficiency. It helps to detect signals that may not be purely sinusoidal, since it would only show up strongly at the fundamental frequency. In contrast, more complex signals with sharper features will have significant power at the higher harmonics.

The Z_3^2-test, or the Rayleigh test, is typically used in X-ray pulsar astronomy, since the phase profiles usually contains sharp pulsation, or even double-peak profiles. One can rewrite Equation (51) using $m = 3$ as:

$$Z_3^2 = \frac{2}{N}\left[\left(\sum_{i=1}^{N}\cos(2\pi\theta_i)\right)^2 + \left(\sum_{i=1}^{N}\sin(2\pi\theta_i)\right)^2\right. \tag{54}$$

$$+\left(\sum_{i=1}^{N}\cos(4\pi\theta_i)\right)^2 + \left(\sum_{i=1}^{N}\sin(4\pi\theta_i)\right)^2 \tag{55}$$

$$\left.+\left(\sum_{i=1}^{N}\cos(6\pi\theta_i)\right)^2 + \left(\sum_{i=1}^{N}\sin(6\pi\theta_i)\right)^2\right], \tag{56}$$

where θ_i are the ith phase in the range from $(0, 2\pi)$ computed using a trial frequency and derivative. The Z_3^2-test algorithm, first, define an array of frequencies to scan. Then, one folds the data and obtains the Z_3^2 value for each case. At the end, the pair of f and $\dot{f}$ that has the highest values is selected.